Impact of Satellite Viewing Swath Width on Global and Regional Aerosol Optical Thickness Statistics and Trends

Peter R. Colarco[1], Ralph A. Kahn[2], Lorraine A. Remer[3], Robert C. Levy[2]

[1]Atmospheric Chemistry and Dynamics Laboratory (Code 614), NASA Goddard Space Flight Center, Greenbelt, MD 20771

[2]Climate and Radiation Laboratory (Code 613), NASA Goddard Space Flight Center, Greenbelt, MD 20771

[3]Joint Center for Earth Systems Technology, University of Maryland-Baltimore County, 5523 Research Park Dr., Suite 320, Baltimore, MD 21250

Abstract

We use the Moderate Resolution Imaging Spectroradiometer (MODIS) satellite aerosol optical thickness (AOT) product to assess the impact of reduced swath width on global and regional AOT statistics and trends. Ten different sampling strategies are employed, in which the full MODIS dataset is sub-sampled with various narrow-swath (~400 – 800 km) and curtain-like (~10 km) along-track configurations. Although view-angle artifacts in the MODIS AOT retrieval confound direct comparisons between averages derived from different sub-samples, careful analysis shows that with many portions of the Earth essentially unobserved, the AOT statistics of these sub-samples exhibit significant regional and seasonal biases. These AOT spatial sampling artifacts comprise up to 60% of the full-swath AOT value under moderate aerosol loading, and can be as large as 0.1 in some regions under high aerosol loading. Compared to full-swath observations, narrower swaths exhibit a reduced ability to detect AOT trends with statistical significance, and for curtain-like sampling we do not find any statistically significant decadal-scale trends at all. An across-track sampling strategy obviates the MODIS view angle artifact, and its mean AOT converges to the full-swath mean values for sufficiently coarse spatial and temporal aggregation. Nevertheless, across-track sampling has significant seasonal-regional sampling artifacts, leading to biases comparable to the curtain-like along-track sampling, lacks sufficient coverage to assign statistical significance to aerosol trends, and is not achievable with an actual narrow-swath or curtain-like instrument. These results suggest that future aerosol satellite missions having significantly less than full-swath viewing are unlikely to sample the true AOT distribution well enough to determine

decadal-scale trends or to obtain the statistics needed to reduce uncertainty in aerosol direct forcing of climate.

1. Introduction

The direct and indirect effects of aerosols remain the largest uncertainties in estimates of the anthropogenic forcing of Earth's climate system (Solomon et al., 2007). Although a conceptually simpler problem than the indirect effects of aerosols on clouds, the direct effect due to scattering and absorption of radiation itself remains poorly constrained owing to uncertainty in aerosol loading, temporal and spatial distribution, and physical properties (Loeb and Su 2010, Kahn 2012). The uncertainty in the anthropogenic direct aerosol radiative forcing component drives much of the uncertainty in overall anthropogenic climate forcing for current climate models (Kiehl 2007).

Attempts to quantify aerosol properties from satellite observations have been made since the 1970s, albeit generally with instruments not optimized for observing aerosols. Since the late 1990s, a suite of satellite instruments designed to measure aerosol properties has helped refine estimates of aerosol loading, and has contributed some progress on retrieving other properties (e.g., absorption, particle size, shape, and vertical distribution) (see CCSP 2009 and references therein). Despite these advances, uncertainties remain, and further reduction of the direct aerosol radiative forcing uncertainty requires improved satellite coverage, as well as integration with *in situ* observations of aerosol type and transport models for synthesis (Diner et al., 2004, Anderson et al., 2005, Kahn 2012).

Spatial coverage is among the primary considerations for any future satellite instrument designed to measure aerosols. Given technological and budgetary constraints, trade-offs are made between spatial coverage (i.e., measurement swath width) and other instrument measurement characteristics, including the number of spectral and polarized channels, relative precision and accuracy, angular and temporal coverage, and pixel size. Furthermore, no one single instrument can provide all desired measurements. A passive, imaging sensor would be aimed at retrieving information about column integrated aerosol loading and composition, and potentially near-source aerosol plume height from multi-angle stereography. Obtaining vertically resolved aerosol amount and type distributions would require an additional, complementary sensor, such as a high-spectral-resolution lidar, likely providing information only along a very narrow, sub-satellite swath.

In this paper we assess the implications of swath width choice for an imaging-type sensor for sampling a single aerosol parameter—the aerosol optical thickness (AOT), a proxy for aerosol column loading—assuming all other factors are held constant. We focus on the AOT because to first order it determines the direct aerosol radiative forcing (DARF) of climate. For example, Hansen et al. (1995) suggest that a change in the global mean AOT of 0.01 corresponds to a climatically important change in the global mean radiative forcing of 0.25 W m^{-2}. This can be compared with the 0.5 ± 0.4 W m^{-2} Intergovernmental Panel on Climate Change (IPCC) stated uncertainty in the magnitude of the anthropogenic DARF component (Solomon et al., 2007). Other analyses suggest that the actual uncertainty is far larger than the IPCC estimate (McComiskey et al., 2008; Loeb and Su 2010). If spatial sampling artifacts introduce sufficient uncertainty in the satellite-derived AOT, we will not be able to meaningfully improve estimates of DARF. It is thus our objective to explore and to characterize these sampling artifacts and their potential impact on AOT.

2. Methodology

2.1. A Conceptual Illustration of the Spatial Sampling Problem

At any given time, nature presents us with a particular three-dimensional spatial distribution of clouds and aerosols, as well as the attendant variability in particle microphysical characteristics, surface reflectivity, and solar illumination. The passive satellite instrument retrieval problem amounts to inverting a meaningful geophysical quantity (e.g., AOT) from this complexity, given a limited set of measured parameters (e.g., backscattered spectral reflectance). Our hypothesis is that the ability to tease out the climatically significant portion of this signal for synoptically important events depends in part on the spatial and temporal coverage of the observing system. In this paper we focus on spatial coverage as determined by the sensor's viewing swath width.

We illustrate the spatial coverage aspects of the problem conceptually in Figure 1. Here, the "true" scene that nature provides (Figure 1d) is sampled by three notional coverage patterns derived from a single day's orbit of the NASA Moderate Resolution Imaging Spectroradiometer (MODIS) instrument aboard the Aqua spacecraft. The underlying image is discernable from the daily sampling only when the full swath MODIS observations are included (Figure 1c). Orbital gaps, clouds, and bright desert surfaces (where the MODIS "dark target" land retrieval is not applied) are readily apparent. The "full-swath" MODIS observations in Figure 1c are then sub-sampled along a hypothetical "narrow" swath (Figure 1b) and a "curtain" swath (Figure 1a). This sampling construction is formally developed in Section 2.3. Figure 1 illustrates that very different pictures of the "true" scene emerge depending on the spatial coverage of the observing system. In what follows, we quantify the impact of spatial coverage characterizing the time varying global and regional field of AOT.

2.2. The Moderate Resolution Imaging Spectral Radiometer (MODIS)

We use aerosol observations from the space-based MODIS instrument for our study. MODIS provides near-global, daily AOT retrievals over land and ocean surfaces. There are two MODIS instruments, both in sun-synchronous polar orbits. MODIS on the Terra satellite has been operational since early 2000 and has a daytime equator crossing time of about 10:30 AM local at the center of its swath. MODIS on the Aqua satellite has been operational since mid−2002 and has a daytime equator crossing time of about 1:30 PM local. At the nominal orbit altitude of 704 km, the MODIS instruments observe a swath about 2300 km wide along their ground tracks. The MODIS orbit is such that the ground coverage is repeated exactly every 16 days. AOT is retrieved in the daytime portion of the MODIS orbit under cloud-free and glint-free conditions using separate aerosol retrieval algorithms for ocean (Tanré et al., 1996, 1997) and land (Levy et al., 2007a, 2007b). In our analysis, we use the land and ocean AOT retrievals from the MODIS Aqua instrument, valid at 550 nm, from the Collection 5 MODIS algorithm products (Remer et al., 2005, 2008; Levy et al., 2010). The retrievals are made at a nominal 10 x 10 km^2 spatial resolution at nadir. A quality assurance (QA) flag is reported for each retrieval, indicating its estimated level of confidence as a valid result, from tests performed during the retrieval process. QA flags range from 0 (lowest confidence) to 3 (highest confidence). In order to retain the highest quality MODIS data, in what follows we use only the highest confidence (QA = 3) retrievals over land, and require QA > 0 for ocean (Remer et al., 2008). The uncertainty in the MODIS AOT (τ) product is characterized such that one standard deviation (66%) of the retrievals fall within $\Delta\tau = \pm0.03 \pm 0.05\tau$ over the ocean and $\Delta\tau = \pm0.05 \pm 0.15\tau$ over land relative to the AOT from coincident ground-based AERONET sun photometer network observations (Remer et al., 2005).

2.3. Sub-Sampling AOT from the MODIS Full Swath

Our spatial sampling strategy is illustrated in Figure 2, which shows an example over-ocean scene comprising a single MODIS Aqua swath. We consider the AOT retrieved across the MODIS full swath (FS), as well as several sub-sampled swaths in which we retain only the relevant portions of the full swath. Four narrow swaths (N1, N2, N3, and N4) are chosen to approximate the ~380 km wide swath of the Multi-angle Imaging Spectroradiometer (MISR, on the Terra spacecraft, Diner et al., 1998). We also consider a "mid-width" swath (MW) with coverage between the narrow and full swath composed of the union of N1 and N2. To approximate the curtain-like sampling of an instrument such as the Cloud Aerosol Lidar with Orthogonal Polarization (CALIOP, aboard the CALIPSO spacecraft, Winker et al., 2010) we consider the samplings C1, C2, C3, and C4, which are extracted at the center of the N1, N2, N3, and N4 swaths, respectively. We emphasize that in all that follows, we are using only MODIS AOT retrievals, sub-sampling the full dataset along the indicated narrow and curtain swaths. The sampling strategies are summarized in Table 1.

The individual retrievals are aggregated onto several regular latitude-longitude spatial grids typical of the grids used in global aerosol transport models. We consider the following spatial resolutions: (a) 10° x 10°, (b) 2° x 2.5°, (c) 1° x 1.25°, and (d) 0.5° x 0.625°. For each, the grid-averaged AOT is:

$$\tau_{grid} = \frac{\sum_{i=1}^{n} \tau_i \cdot q_i}{\sum_{i=1}^{n} q_i} \tag{1}$$

where τ_i are the 1 through n individual AOT retrievals falling into the grid box and q_i is the QA value assigned to each retrieval. Our aggregation is thus QA weighted. Over land we have only retained QA = 3 retrievals, based on the MODIS Aerosol Product Data Quality Statement. The aggregation is performed daily. The temporally averaged (e.g., monthly, seasonal, annual) AOT at a grid box is:

$$\langle \tau \rangle = \frac{\sum_{j=1}^{m} \tau_{grid,j} \cdot n_j}{\sum_{j=1}^{m} n_j} \tag{2}$$

where $\tau_{grid,j}$ is the grid average value at day j from Equation 1 and n_j is the number of retrievals used to make $\tau_{grid,j}$. This aggregation and weighting strategy is the same as in Remer et al. (2008) and Colarco et al. (2010).

3. Results

3.1. The Sub-Sampled AOT

The sub-sampled MODIS Aqua data are analyzed for the years 2003 – 2012. Figure 3 shows an example of the year 2010 annually averaged AOT from the full swath MODIS Aqua retrievals over both land and ocean using the aggregation strategy given by Equations 1 and 2. Each of our four aggregation spatial resolutions is illustrated. In general, the spatial patterns of the main aerosol features are coherent among the different resolutions: the Saharan dust and Asian pollution and dust outflow plumes, the biomass burning activity over southern Africa and South America, the pollution plume over China, the band of high AOT in the southern ocean, and a region of high AOT over western Russia where a significant biomass burning anomaly occurred in 2010 (Witte et al., 2011).

An exception to this coherence in the pattern is particularly evident at the coarsest (10° x 10°) spatial resolution map over northern Africa (Figure 3a). The MODIS dark target land retrieval does not make retrievals over bright land surfaces such as desert or snow and ice, and indeed at the higher spatial resolutions the Sahara is generally devoid of AOT retrievals. To the extent that the few retrievals made in these regions fall into one of our 10° x 10° grid boxes, the entire box acquires a value propagated through to the annual mean (i.e., in this illustration, we did not exclude any grid boxes for having only a small number of retrievals). Additionally, we have applied a simple mask in combining the land and ocean retrievals into a single map in Figure 3. Where the same grid box has both land and ocean retrievals in it we have retained the ocean retrieval only (i.e., we do not attempt to combine land and ocean together). That we are making this choice is most apparent at the coarsest spatial resolution, and it is of much less importance as higher spatial aggregation resolutions are considered.

Figure 4 shows the same annually averaged AOT for the year 2010, but now for four of the sub-sampling strategies discussed above. Here we show aggregate maps at our highest spatial resolution (0.5° x 0.625°) only, and show two narrow (N1 and N3) and two curtain-like (C1 and C3) samplings. As seen in Figure 2, N1 and C1 are on the eastern edge of the MODIS swath, whereas N3 and C3 are down the center of the swath. Because of sunglint, N3 and C3 have relatively poor retrieval sampling over the tropical ocean, especially evident in C3, for which a wide band of essentially no retrievals occurs around the equator. We emphasize that in Figure 4 the approach is "sample-then-average," and so is done on a "per-orbit" basis (see Table 1). Only the MODIS retrievals that could have been sampled are pulled from the full swath dataset, then aggregated, and then finally averaged. This "sample-then-average" approach is how time averages are typically calculated from polar orbiting satellite datasets. We make this point to distinguish from a different sampling approach discussed later (Figure 8).

Many of the features apparent in the full swath annual mean in Figure 3 are still apparent in Figure 4: the biomass burning plumes over South America and southern Africa, the Asian outflow across the northern Pacific, Saharan dust transport across the North Atlantic, and dust and anthropogenic pollution over India and China. On the other hand, the shapes and apparent magnitudes of these features are clearly different, and certain features are notably absent, particularly the Russian fires in the C1 and C3 samplings, the Saharan dust plume in the C3 sampling (mostly in the glint region), and the high AOT features over the southwest United States in the C1 and N1 samplings.

Figure 5 shows the years 2003 – 2012 time series of global, annual mean AOT over both land and ocean for each of our sampling strategies generated with a similar procedure to what is shown in Figure 4. The full swath annual mean AOT varies between about 0.13 and 0.14 over the ocean and about 0.16 and 0.18 over the land, similar to the multi-year analysis presented in Remer et al. (2008). We compare the global, annual mean AOT of our various sampling strategies to the full swath AOT. Over ocean, except for the N4 and C4 samplings, the global, annual mean AOT is within 0.01 of the full swath value. Over land, most of the sampling strategies differ from the full swath by more than 0.01 at some point in the time series, with N1 and C1 notably underestimating the global, annual mean AOT relative to the full swath.

Figure 5 shows that there are sometimes large differences even in the global, annual mean AOT resulting from the different spatial sampling of the MODIS dataset. This is important, because if the narrow-swath or curtain-like sampling cannot reproduce the basic statistics of the full swath AOT even at the global and annual scales, the question of whether we can rely on this measurement strategy for narrowing the uncertainties in key aerosol properties and their impacts on climate must be assessed quantitatively.

There is, however, a significant caveat to the results presented in Figure 5. Although the differences between, say, the C1 sub-sample and the full swath AOT certainly contain a component related to the spatial sampling, errors and uncertainties in the MODIS retrievals themselves also contribute to the observed differences. In particular, the MODIS AOT retrieval has a sensor view-angle dependency (Levy et al., 2010). That is, if the aerosol loading is homogeneous across the MODIS swath, different AOT values will under some circumstances nevertheless be retrieved in different positions across the swath, owing to this angular artifact. However, the characteristic of that artifact as a function of view angle, sun angle, position on Earth, surface reflectance, etc., is not well understood. In an earlier study on the sampling question posed here (Colarco et al., 2012) we attempted to correct for this dependency by examining a dataset of MODIS-AERONET collocations sorted by view geometry, similar to what is shown in Levy et al. (2010) (see, for example, their Figure 10). This proved challenging. The collocation dataset was relatively small and was only available where AERONET sites are located. The latter point made it difficult to evaluate the view angle dependency of the MODIS AOT retrievals, especially over ocean. The dataset would have been smaller still for determining these view angle dependencies on a seasonal or regional basis. For these reasons, we could not separate view angle from spatial sampling differences when the full swath and sub-sample AOT datasets were compared, so we here take a different approach to evaluate the impact of swath width on global AOT statistics.

3.2. Observability and Regional Analyses

Although we cannot correct the MODIS observations for the view angle dependency with confidence, we can investigate the question of observability: what are the characteristics of the observations that are *not* made in a given sub-sample, and how does this impact the derived AOT statistics?

Figure 6 complements Figures 3 and 4. It shows the 2010 full swath annual mean AOT from Figure 3d, but only in grid boxes where the indicated sub-sampling strategy had no valid annual mean AOT (i.e., in grid boxes where the sub-sample either never visited because of coverage limitations, or else never encountered a good AOT retrieval because of algorithmic issues when it did overfly the grid box). Similar to Figure 4, we show this for N1, N3, C1, and C3 sub-samples. This is revealing. The N1 and N3 figures show that, like the full-swath sampling, the narrow-swath sampling permits retrieval of AOT over most points on Earth at least once during the year. However, in some places where the full swath sampling would have made relatively few observations, the narrow-swath sampling provides no observations at all. (Figure 7 shows, for example, the total number of retrievals in each grid cell that comprise the year 2010 full-swath annual mean.) These regions are generally where seasonal changes in surface brightness due to vegetation (e.g., the US southwest, the Sahel) or seasonal snow cover (the Tibetan plateau) make retrieval difficult and thus less frequent. On the other hand, Figure 6 illustrates something qualitatively different when only curtain-like sampling is obtained: it is clear that much of the Earth is never visited at all under this sampling.

In our analysis of observability, to reduce the issue of the view angle artifact discussed above we create what we call our "average-then-mask" strategy (Table 1). First, we construct monthly, seasonal, or annual mean maps of the AOT from the full swath data, effectively sampling the location at all viewing geometries obtained by MODIS. Second, we create masks that mark out the grid boxes observed by each sampling strategy over the relevant averaging period. Finally, we apply the masks to the aggregated maps of the full swath AOT. This "average-then-mask" strategy is in contrast to the "sample-then-average" strategy described in Section 2.3.

The results of this method provide a view of the features each sampling strategy can observe, and estimates of the mean AOT differences that are unbiased by scan angle artifacts. But it also represents a much richer data set than could be obtained from an instrument having similar retrieval capabilities to the full swath MODIS but having only narrow or curtain sampling. As a result, this method reduces significantly the difference in AOT variability measured by the different sampling strategies compared to the difference obtained using the "sample-then-average" method. This reduction in the variability is illustrated in Figure 8, which shows again the time series of annual mean AOT over the ocean and land for each sub-sampling strategy, but now using the "average-then-mask" approach. It is clear that in the global, annual mean, the AOT for the sub-samples generally differs from the full swath value by much less than 0.01. However, *the "average-then-mask" approach for the curtain-like cases provides spatial sampling that would never be acquired by an actual curtain instrument*, because they come from different parts of the broad MODIS swath. So although this approach minimizes the view-angle bias, it includes much greater sampling than would be available from a curtain instrument.

Using this "average-then-mask" method, we emphasize the issue of observability further in Figure 9, where we zoom in on the key aerosol features in the region surrounding the tropical Atlantic Ocean, focusing on the seasonal AOT for the period July-August-September 2010. We show the MODIS full swath seasonal mean AOT at grid cells both where C1 and C3 do and do not observe (i.e., the union of the two C1 sampling images, Figures 9a and 9b, yields the full swath seasonal mean for this region, as does the union of the two C3 sampling images, Figure 9c and 9d). Here the spatial gaps in the curtain-like sampling become more apparent, and visual inspection of the figures reveals differences in the patterns of the aerosol features seen. For example, the AOT features over the Nile River valley are nearly absent in the C1 and C3 sampling (Figures 9a and 9c) but are readily apparent when looking at the grid cells unobserved by these sampling strategies (Figures 9b and 9d). Likewise, the shape of the biomass burning plume over South America is more apparently filled in for the grid cells unobserved by C1 and C3 (again, Figures 9b and 9d). Most readily apparent is the wide equatorial belt over the ocean, encompassing the Saharan dust plume, where the C3 sampling is almost completely absent due to glint (Figure 9c versus 9d). Even for the C1 sampling, where the ocean glint is not an issue in this case, the South African biomass burning plume is also missing some of the highest-AOT regions when the observed and unobserved grid cells are compared (Figures 9a and 9b).

A similar analysis is presented in Figure 10 over the Asian region for the March-April-May 2010 seasonal average. Here we show only the C1 sub-sample masking. Aerosol features over Iraq, Iran, Turkmenistan, Afghanistan, northern China, and the Sichuan Basin in central China are almost completely unobserved by the C1 sampling (Figure 10a), and the pattern of the main Asian outflow over the northern Pacific is much less well defined.

For AOT trend and regional climate impact studies, quantitative differences matter. We assess the quantitative differences produced by different sampling strategies for several regions exhibiting major aerosol features as highlighted with white boxes in Figures 9 and 10. In Figure 11, for each of the regions highlighted in Figures 9 and 10 we compute the time series of the difference in the regional mean AOT due to sampling. That is, for each region and season we find the full swath regional AOT and the "average-then-mask" regional AOT for each sub-sample. The ΔAOT shown is the difference between the maximum and minimum AOT for all ten sampling strategies, including the full-swath average. Because the glint significantly impacts the sampling in the C3 and N3 sub-samples for certain regions, we also show the ΔAOT excluding C3 and N3 (dashed lines). This restriction is especially important for the Southern Africa, African Dust, Nile River, Southeast Asia, and Asian Outflow regions. To highlight the differences between curtain-like and narrow-swath sampling we show the ΔAOT for the full swath, C1, C2, and C4 samplings only (blue line) and for the full swath, N1, N2, and N4 samplings only (red line). For all, we additionally show the full swath AOT value and the magnitude of ΔAOT (in all cases, the ΔAOT excluding the C3 and N3 samples) as a fraction of the seasonal-regional full swath AOT. Finally, the r^2 correlation coefficient of the ΔAOT (again, excluding C3 and N3) with the full swath AOT and the fraction of the full swath are also indicated.

We refer to ΔAOT as the "sampling artifact," as it shows the uncertainty in the seasonal-regional AOT due to spatial sampling issues. We note that for all regions the ΔAOT sampling artifact is highest for the curtain-like sampling (blue line), and so drives the sampling artifact for all sampling strategies (black dashed line). The ΔAOT artifact is strongly affected by the glint-impacted sub-samples (C3 and N3). This is especially evident for the African dust and Asian outflow regions, where there is essentially no sampling artifact if the glint-impacted sub-samples are excluded. The glint impact is also evident in Southern Africa, the Nile River, and Southeast Asia, although in these regions there remain significant sampling artifacts.

The South America region (Figure 11a) shows significant annual and inter-annual variability in the full swath AOT, with a peak AOT of between 0.2 and 0.4 typically occurring in JAS or OND associated with seasonal biomass burning. This peak is modestly correlated ($r^2 = 0.25$) with the ΔAOT, which can be as high as 0.06. Because this region is over land, it is not significantly affected by the C3 and N3 sunglint-related sampling biases. Interestingly, ΔAOT is uncorrelated with its fractional comparison to the full swath AOT, although as a fraction of the full swath AOT the ΔAOT typically peaks at 40% and can be as high as 60%. Thus, for South America, the uncertainty in AOT due to sampling may be as much as 0.06, comprising ~15% of a base magnitude as high as about 0.4, and can also represent uncertainties as great as 60% in the regional AOT when AOT is lower.

In Southern Africa (Figure 11b) the glint-affected C3 and N3 samplings introduce significant bias in the ΔAOT. This is another region affected by seasonal biomass burning, with peak AOT of about 0.4 occurring in JAS. Excluding the C3 and N3 samples, the peak ΔAOT is at most 0.03 and is weakly correlated with the full swath AOT ($r^2 = 0.14$), but much more strongly with the fractional contribution ($r^2 = 0.72$).

For African Dust (Figure 11c) the C3 and N3 samplings are determinant, and excluding these, the ΔAOT is small (approximately 0.01) and is consistently less than about 5% of the magnitude of the full swath seasonal-regional AOT. In other words, for the African Dust region, the average-then-mask sampling does not significantly impact these AOT statistics. For the Nile River (Figure 11d) the C3 and N3 are similarly important drivers. Excluding these, the ΔAOT is at most about 0.05 and is modestly correlated ($r^2 = 0.37$) with the full swath seasonal-regional mean AOT signal. The full swath mean AOT has a seasonal signal, varying between about 0.2 and 0.4 in magnitude, and the sampling artifact may be as much as about 20% of the full swath value.

Turning to Asia, for the Indogangetic Plain (Figure 11e), the ΔAOT is mostly unaffected by the C3 and N3 samples. Peak values of ΔAOT are as high as 0.1 but are uncorrelated with the full swath AOT, which itself peaks in magnitude at about 0.5. The sampling artifact may thus be as much as about 30% of the full swath signal. Similarly, in China (Figure 11f), the C3 and N3 samplings do not greatly affect the analysis. The ΔAOT is as high as 0.09 and is sometimes as large 20% of the full swath mean AOT, which itself varies between about 0.3 and 0.6 in magnitude. By contrast, the Southeast

Asia (Figure 11g) and Asian Outflow (Figure 11h) regions are strongly impacted by the C3 and N3 sampling. Excluding these, the peak ΔAOT values are 0.05 and 0.015, respectively. For Southeast Asia, this sampling artifact can be as large as 20%, but is mostly less than 10% of the full swath signal. The contribution to the Asian Outflow signal is negligible, with sampling introducing an uncertainty of only about 5% at most for a full swath AOT that peaks above 0.4 in magnitude.

In summary, with the "average-then-mask" approach, differences are due solely to sampling, as we are only comparing the data set with sub-samples of itself, and cross-swath anomalies are removed by the averaging. In addition, the average-then-mask approach incorporates much greater sampling than actual reduced-swath instruments can obtain – about three-to-four times more samples for the narrow-swath, and about 16 times more samples for the curtain. However, significant qualitative and quantitative differences still appear in the seasonal, regional average AOT distributions; minima and maxima do not capture the extreme values, and some regional features are entirely missed. Due to the much greater sampling included in the "average-then-mask" data, results presented in Figures 8-11 are significantly more favorable than would be produced for instruments having such spatial sampling characteristics, and thus the sampling artifacts presented in this section are effectively lower bounds. The overall magnitude of the sampling artifact is largest for the curtain-like sub-samples, as might be expected. The nature of this artifact is such that in some regions (South America, Indogangetic Plain, China) it can be as large as 60% of the full swath AOT signal or as great as 0.1 in AOT magnitude.

3.3. Trends in Aerosol Optical Thickness

In the previous section we showed that in some regions significant artifacts are introduced in the seasonal-regional mean AOT when the full swath data are sub-sampled. These artifacts increase the uncertainty in seasonal estimates of climate-relevant factors such as aerosol loading and radiative forcing. In addition to these seasonal "snapshots" of the aerosol loading, the temporal evolution of aerosol loading is also of major interest. In this final section of results we ask how spatial sampling affects the ability to detect statistically significant AOT trends.

Our approach follows the trend analysis presented in Zhang and Reid (2010), which employs the statistical tools of Weatherhead et al. (1998) to assess confidence levels in the derived trends. Briefly, a linear model is fit to the monthly mean AOT time series at a grid box. A first-order autoregressive "noise" model characterizes the residual of the observed time series from the linear model. The slope of the linear fit, ω, is the trend in the time series, and the standard deviation of the trend, σ_ω, is defined in terms of the variance of the residual noise model (see Equation 2 in Weatherhead et al., 1998). Where the ratio $|\omega/\sigma_\omega| > 2$ the trend is statistically significant at the 95% confidence level (Weatherhead et al., 1998).

In Figures 12 – 14 we illustrate the application of this methodology to our ten-year (2003 – 2012) full swath and sub-sampled extractions of the MODIS data set. We use the monthly mean aggregations from our "sample-then-average" approach for this analysis, as it more realistically represents the data that would be acquired by a narrow-swath or curtain instrument. As in Zhang and Reid (2010), the AOT time series is deseasonalized before the linear model is fit, because the seasonal aerosol signal is so large in many parts of the world. Our “sample-then-average” approach may contain scan angle biases in the AOT field itself that could alias the magnitude of the derived AOT at some locations. However, this will not affect the statistical significance of the derived trends as long as whatever scan angle artifacts exist they do not vary over time for a given sub-sample of the MODIS swath. The high calibration stability of the MODIS instruments (Xiong et al., 2006) supports this assumption, although a calibration drift in certain MODIS channels does affect the Collection 5 MODIS AOT data (Levy et al., 2010). For the purpose of the current study, we are concerned primarily with differences in the statistical significance of the trends that can be derived for various distributions of samples.

Figure 12 shows the AOT trend for the full swath, mid-width, N1, and C1 samplings. The full swath (Figure 12a) shows strong decreasing trends in AOT over the Amazonian region in South America and in eastern-central Siberia, and moderate decreasing trends across the eastern United States and Canada and the western North Atlantic Ocean, Europe and the Mediterranean, in the Gulf of Guinea and off the west coast of Northern Africa, and in the western Pacific around the Maritime Continent. Strong positive trends are apparent in the Arabian Sea, across India, and in the Bay of Bengal, in Iraq, off the western coast of southern Africa, across Sudan and Ethiopia, near Beijing in eastern China, in eastern central Argentina, and in eastern Siberia and across the northern Pacific Ocean. Moderate positive AOT trends are seen in the western United States and Canada, over southern Africa, and more generally across northern Asia. Except as noted previously, the oceans generally have no trend in AOT or else a weakly positive trend. The locations and signs of our computed trends are generally similar to

Zhang and Reid (2010, their Figure 7a), although we note that they restricted their analysis to over-ocean regions only, covered a shorter time period, and used their "assimilation-grade" version of the MODIS AOT product, which is quality controlled as described in Zhang and Reid (2006). Our trends differ from theirs primarily in the Pacific west of Mexico, where we show a slight increasing trend and they show a weak decrease.

The mid-width sampling trends (Figure 12b) are generally similar in magnitude and sign to the full swath trends. The N1 sampling trends (Figure 12c) are also similar in pattern and sign to the full swath trends, but differences from the full swath are more clearly visible, including a stronger positive trend associated with the southern African biomass burning plume and a more strongly negative trend across central western Africa and in northeastern Asia. The lesser coverage associated with the C1 sampling makes the trends harder to discern for that case (Figure 12d), although the overall patterns of increasing and decreasing trends are again fairly consistent with the full swath. The other narrow and curtain-like samples have similar trend patterns and magnitudes (not shown), but differ in detail, and the N3 and C3 samples have poor coverage over the tropical oceans.

The differences in the trend magnitudes between our sampling approaches are not unexpected. Zhang and Reid (2010) found, for example, weaker magnitude for trends from MISR observations than for MODIS. Zhang and Reid (2010) attributed this difference in the MODIS and MISR trends at least in part, if not entirely, to the lower spatial coverage of MISR. Additionally, our "sample-then-average" approach can affect the magnitudes of the trends, due to MODIS view-angle biases discussed previously.

Our focus is thus on our ability to assign statistical significance to whatever trend appears in the maps.

In Figure 13 we present the spatial distribution of statistical significance for the trends shown in Figure 12. For the full swath (Figure 13a) our analysis shows that the computed trends are significant at the 95% level broadly across the tropical Pacific Ocean, in the Arabian Sea and Bay of Bengal, in the Mediterranean, and then across Sudan and Ethiopia and into the western Indian Ocean. Our patterns for significance are again similar to those of Zhang and Reid (2010) (their Figure 7b), except that their broad region of significance between southern Africa and South America is much less pronounced in our analysis. Over land we find statistical significance in the full swath for southern India, near Beijing, across the central United States, in Argentina, and across portions of the biomass burning region in Amazonia.

The over-ocean patterns of significance are nearly identical in the mid-width (MW) sampling (Figure 13b), but over land there are notable differences, with MW indicating no significance in the trends over Amazonia, in China, or in the central United States. The regions of significance in the trends over India and in the Sudan and Ethiopia area are much reduced in area. This reduction in areal extent of significance patterns worsens for the N1 sampling (Figure 13c), with significance essentially gone over Sudan and Ethiopia, and as well being much reduced over Argentina. The patterns over ocean are still generally similar to the full swath, but the individual regions are less coherent. For the C1 sampling (Figure 13d) the statistical significance at the 95% confidence level is essentially gone, with nothing identifiable over land and only a hint of significance in the tropical Pacific and in a few other ocean regions. The patterns of significance for the other narrow and curtain-like samplings (not shown) are similar to the N1 and C1 shown in Figure 13, respectively, though different in detail. N2 and C2 have somewhat better coverage over the oceans. N3 and C3—again, because of the glint— show poor coverage over the oceans. C4 in particular has far worse coverage over the ocean than C1.

4. Discussion and Conclusions

We have investigated the impact of spatial sampling on the statistics of the MODIS AOT. We showed significant differences in the global, annual mean AOT arrived at as a function of our sampling strategy (Figure 5). The "sample-then-average" approach employed, however, could not disentangle the spatial sampling artifacts (which we are most interested in isolating) from the sensitivity of the MODIS AOT retrieval to viewing geometry. Subsequently, we considered instead the observability problem: where the sub-sample could have obtained aerosol retrievals, where it could not, and where—compared to the full-swath values—important differences in the regional and seasonal AOT are inferred. The "average-then-mask" approach (Section 3.2) mitigates biases associated with location in the MODIS swath, but greatly increases the sampling compared to an actual instrument having a narrower swath, because the full swath MODIS instrument obtains much more frequent observations of any given location than an actual narrow-swath instrument would. This approach yielded global, annual mean AOT values that were insignificantly different from the full-swath AOT values (Figure 8), in contrast to what was shown in Figure 5.

For several regions with important aerosol features, we calculated a "sampling artifact," shown graphically in Figure 11, illustrating deviations in the seasonal-regional mean AOT due to spatial sampling considerations. The sampling artifacts were small for our more ocean-influenced regions, but could be as large as 0.1 in the seasonal AOT for high-loading, near-source regions such as China and the Indogangetic Plain. As a percentage of the full-swath seasonal, regional mean AOT, the sampling artifact could be as large as 60% (South America), and was in many places of order 20% (China, Indogangetic Plain, Nile River). In almost all cases the magnitude of the sampling artifact was largest for the curtain-like sampling, with smaller artifacts inferred when the narrow-swath sampling was compared to the full swath, as might be expected. The "average-then-mask" strategy applied to the regional analysis discussed here is a lower bound on the actual sampling artifact because this approach actually draws from the full swath observations and simply excludes places *never* observed by the sub-sample.

We additionally investigated our ability to detect statistically significant trends in aerosol features as a function of spatial sampling. Although the signs of the trends were similar for the various sampling strategies employed, magnitudes were in some places quite different. This is attributable in part to the MODIS view angle bias, but also to differences in the spatial coverage. Again, most places on Earth are simply never observed with curtain-like sampling, including some major aerosol source regions. That reduced spatial coverage had a profound impact on the ability to assign statistical significance to the trends (Figure 13). For example, even the widest of our sub-samples (MW) could not assign significance at the 95% confidence level (generally used as the criterion for trend detection) to any decadal-scale trends over Amazonia or the central United States, and had reduced confidence in western Africa and India. The patterns of significance were even less coherent for the narrow-swath sampling, and were essentially gone for the curtain-like sampling. Without relying on direct comparison with the significance patterns in the full swath observations, it is not clear what could be said at all about aerosol trends from the curtain-like observations alone.

A recent paper by Geogdzhayev et al. (2013) is of particular relevance to this study, as they provided a similarly motivated analysis of the MODIS AOT data. Their approach was to develop sub-samples by aggregating individual scans *across* the MODIS swath. They argued that this removed the view angle artifact when compared to the full set of MODIS observations, versus a comparison to along-track sampling (i.e., samples similar to our C1-4 sub-samples). This across-track sampling is illustrated for a portion of the MODIS Aqua orbit in Figure 14a (compare with our along-track sampling shown in Figure 2).

We implemented this sampling approach in the same framework as the along-track samplings discussed earlier, selecting five evenly spaced across-track sub-samples (L1, L2, L3, L4, and L5, with the "L" standing for "latitudinal"). The year 2010 annual mean AOT for the L1 sub-sample is shown in Figure 14b. When compared with the full swath annual mean AOT (Figure 3d) we see a lot of "noise" (small-scale variability) in the AOT field for the L1 sub-sample. Consistent with the earlier discussion of our along-track sub-samples, there are important aerosol features missed by this sampling, including the South American biomass burning plume and the Russian fires. Nevertheless, when the global, annual mean AOT is compared to the full swath AOT, there is essentially no difference between any of the latitudinal sub-samples and the full swath (Figure 14c, shown for ocean, but the results are essentially the same over land). This result is consistent with Geogdzhayev et al. (2013).

When considering the seasonal-regional statistics, however, it is clear a significant spatial sampling artifact still remains in the across-track sampling, as might be expected from the small-scale variability in the map of global AOT (Figure 14b). Figures 14d and 14e show the across-track sampling seasonal-regional mean ΔAOT for, respectively, South America and the Indogangetic Plain (compare with Figures 11a and 11e). The sampling artifact ΔAOT for the across-track sampling was indeed smaller than for our along-track, curtain-like sampling, but even so, ΔAOT for the across-track sampling is substantial in places. Over South America, the peak ΔAOT is about 0.04, smaller than the peak ΔAOT of 0.06 in Figure 11a, but over the Indogangetic Plain the artifact is roughly the same as shown in Figure 11e. Note that these results were obtained similarly to those shown in Figure 11, from our optimistic "average-then-mask" approach. As the latitudinal sampling should obviate the MODIS view angle bias (Geogdzhayev et al., 2013), generating the seasonal-regional statistics using the "sample-then-average" approach would better represent the observations of an actual curtain instrument. When we tried this, we found the sampling artifact was actually worse in all regions (Figure 15 for South America and Indogangetic Plain).

In Figure 16 we show the AOT trend and statistical significance pattern for the L1 sub-sample. The global distribution of the sign of the trends is generally consistent with the full swath dataset (Figure 12a), but there are considerable differences in coverage. The full swath observations have hundreds-to-thousands of observations per year informing a given grid box (Figure 7), whereas the L1-type sampling has at most a few dozen (not shown). The relatively poor coverage for the L1 sampling at this resolution renders the trend statistically insignificant almost everywhere (Figure 16b). This is also true for the other latitudinal sub-samples (not shown). The particular areas of coverage and trend magnitudes differ somewhat among the different latitudinal sub-samples, but in all cases there is almost no ability to assign statistical significance.

For completeness, we performed this same trend analysis at a coarser 10° x 10° spatial aggregation, compatible with the resolution of the analysis performed in Geogdzhayev et al. (2013). The AOT trends and the map of 95% statistical significance for the full swath, L1, N1, and C1 samplings are presented in Figures 17 and 18, respectively. Results may be compared with Figures 12, 13, and 16. The assignment of statistical significance to a detected trend is of course more robust at the coarser spatial resolution, since relatively more of these larger grid boxes have valid monthly means at the coarser spatial resolution. Thus, unlike what was seen at higher spatial resolution (Figures 16b and 13d, respectively), at 10° x 10° spatial resolution it is possible to assign statistical significance more broadly for the L1 and C1 samples (Figure 18).

Geogdzhayev et al. (2013) suggest that spatial coverage does not matter to the statistics of AOT. We strongly disagree. Their approach certainly reduces the across-track view angle bias in the MODIS AOT retrievals. For sufficiently coarse spatial and temporal averaging scales (e.g., global, annual mean), the cross-track, globally sampled AOT should converge to the full-swath values, as it does. At finer scales (e.g., regional, seasonal means), however, significant sampling artifacts remain, consistent with our analysis of along-track sampling. In addition, the associated estimates of changes in DARF obtained from trends derived at coarse spatial and temporal scales would be complicated by the variability in aerosol single scattering albedo, aerosol vertical distribution, and surface properties across the large grid boxes.

Our conclusion is that spatial sampling matters. Our study shows the limitations of curtain-sampling instruments at capturing the statistics of AOT values at regional scales, compared to the full-swath MODIS observations. It further calls into question the ability of curtain-sampling instruments to reliably detect trends in aerosol loading on decadal time scales. Although the narrow (~400 km) swath sampling fares better, without the context of a full swath imager's observations, there is little confidence in even these derived trends, a conclusion similar to one obtained by Zhang and Reid (2010).

The global aerosol system is temporally and spatially variable, and any realizable sampling and aggregation method applied to observing this system will introduce sampling biases. Simply acquiring a data set with abundant statistics does not guarantee that it will reflect the planet's mean aerosol loading and especially not its variability, nor the radiative perturbation caused by that loading. However, broad-swath sampling maximizes the likelihood of obtaining a representative picture.

Our study establishes the limitations of a curtain instrument having retrieval capabilities similar to those of MODIS. Note that the MODIS data set does not capture all aspects of the actual aerosol field, in part due to contextual limitations of the measurement technique, such as the lack of diurnal observations and the inability to retrieve AOT under and in the immediate vicinity of clouds (e.g., Zhang and Reid, 2009). For these reasons we cannot directly assess the results for a curtain instrument having arbitrarily greater accuracy or fewer spatial gaps caused by unfavorable retrieval conditions. However, even if such an instrument could retrieve aerosol properties with *no* cloud exclusions, it would still be sampling only about ~10% of the globe. In addition to aerosol amount and type, DARF depends strongly on the reflective properties of the surface over which the particles reside, most of which would be unobserved by the curtain instrument. What we do have, however, is MODIS, which represents the best available combination of broad swath, high quality, and long running coverage of satellite-based aerosol properties at our disposal. We find that the full-swath trends in our study actually match the "contextually less-biased" assimilation-grade trends in Zhang and Reid (2010), suggesting that although contextual bias can be an issue, it probably does not diminish the applicability of our conclusions.

An extension of our work here would be to explore the spatial sampling dependencies in the context of a data-assimilation grade instance of the MODIS dataset (e.g., Zhang and Reid 2006) that has been processed to reduce as much as possible MODIS AOT artifacts. A further extension would be to perform similar sampling analyses in the context of a global aerosol transport model, which would obviate the context biases noted above and could help characterize these spatial and temporal sampling dependencies. A significant challenge in that approach, however, is to ascertain how well any aerosol transport model represents actual aerosol variability. Another approach would be to formally assimilate various sub-sampled MODIS data sets into a transport model and investigate the impact on predicted aerosol distributions and radiative forcing. These additional avenues of study would complement the work presented here.

Acknowledgements

This work was funded by the NASA Earth Science Division as part of the pre-formulation study for the Aerosol, Cloud, and ocean Ecosystem (ACE) Mission. We acknowledge Hal Maring, Paula Bontempi, Mark Schoeberl, David Starr, and Lisa Callahan for supporting this work. We thank Rich Ferrare, Alexei Lyapustin, Alexander Marshak, Jeffrey Reid, and Ellsworth Welton for comments on an early version of this manuscript. The image of the Mona Lisa shown in Figure 1 was taken from the website: https://en.wikipedia.org/wiki/File:Mona_Lisa,_by_Leonardo_da_Vinci,_from_C2RMF_retouched.jpg

References

Anderson, T.L., R.J. Charlson, N. Bellouin, et al., 2005: An "A-Train" strategy for quantifying direct climate forcing by anthropogenic aerosols. *Bull. Am. Meteorol. Soc. 86*, 1795-1809.

CCSP (U.S. Climate Change Science Program) Synthesis and Assessment Product 2.3, 2009: Atmospheric aerosol properties and climate impacts. **C**hin, M, R. Kahn, and S. Schwartz, Eds. pp. 116.

Colarco, P., A. Da Silva, M. Chin, and T. Diehl, 2010: Online simulations of global aerosol distributions in the NASA GEOS-4 model and comparisons to satellite and ground-based aerosol optical depth. *J. Geophys. Res.*, **115**, D14207, doi:10.1029/2009JD012820.

Colarco, P.R., L.A. Remer, R.A. Kahn, R.C. Levy, and E.J. Welton, 2012: Implications of satellite swath width on global aerosol optical thickness statistics, *Atmos. Meas. Tech. Discuss.*, 5, 2795-2820, doi:10.5194/amtd-5-2795-2012.

Diner, D., J. Beckert, T. Reilly, C. Bruegge, J. Conel, R. Kahn, J. Martonchik, et al., 1998: Multi-angle Imaging SpectroRadiometer (MISR) - Instrument description and experiment overview, *IEEE Trans. Geosci. Rem. Sens.*, 36(4), 1072–1087.

Diner, D.J., T.P. Ackerman, T.L. Anderson, J. Bösenberg, A.J. Braverman, R.J. Charlson, et al., 2004: PARAGON: An Integrated Approach for Characterizing Aerosol Climate Impacts and Environmental Interactions, *Bull. Amer. Met. Soc.*, 85(10), doi: http://dx.doi.org/10.1175/BAMS-85-10-1491.

Geogdzhayev, I., Cairns, B., Alexandrov, M. and Mishchenko, M. I., 2013: Statistical analysis of single-track instrument sampling in spaceborne aerosol remote sensing for climate research, J Quant Spectrosc Ra, 121, 69–77, doi:10.1016/j.jqsrt.2013.02.003.

Hansen, J., W. Rossow, B. Carlson, A. Lacis, L. Travis, A. DelGenio, I. Fung, et al., 1995: Low-cost long-term monitoring of global climate forgings and feedbacks. *Climatic Change*, **31**(2-4), 247–271.

Kahn, R. A., 2012: Reducing the Uncertainties in Direct Aerosol Radiative Forcing. *Surveys in Geophysics*, doi:10.1007/s10712-011-9153-z.

Kiehl, J. T., 2007: Twentieth century climate model response and climate sensitivity. *Geophys. Res. Let.*, **34**(22), L22710, doi:10.1029/2007GL031383.

Levy, R. C., L.A. Remer, and O. Dubovik, 2007a. Global aerosol optical properties and application to Moderate Resolution Imaging Spectroradiometer aerosol retrieval over land. *J. Geophys. Res.*, **112**(D13), D13210. doi:10.1029/2006JD007815.

Levy, R.C., L.A. Remer, S. Mattoo, E.F. Vermote, and Y.J. Kaufman, 2007b: Second-generation operational algorithm: Retrieval of aerosol properties over land from inversion of Moderate Resolution Imaging Spectroradiometer spectral reflectance. *J. Geophys. Res.*, **112**(D13), D13211. doi:10.1029/2006JD007811.

Levy, R.C., G.G. Leptoukh, R. Kahn, V. Zubko, A. Gopalan, and L.A. Rember, 2009: A critical look at deriving monthly aerosol optical depth from satellite data. *IEEE Trans. Geosci. Rem. Sens.*, **47**(8), 2942-2956, doi: 10.1109/TGRS.2009.2013842.

Levy, R.C., L.A. Remer, R.G. Kleidman, S. Mattoo, C. Ichoku, R. Kahn, and T.F. Eck, 2010: Global evaluation of the Collection 5 MODIS dark-target aerosol products over land. *Atmos. Chem. Phys.*, **10**(21), 10.5194/acp-10-10399-2010.

Loeb, N.G., and W. Su, 2010: Direct Aerosol Radiative Forcing Uncertainty Based on a Radiative Perturbation Analysis. *J. Clim.*, **23**(19), 5288–5293, doi:10.1175/2010JCLI3543.1.

McComiskey, A., S.E. Schwartz, B. Schmid, H. Guan, E.R. Lewis, P. Ricchiazzi, and J.A. Ogren, 2008: Direct aerosol forcing: Calculation from observables and sensitivities to inputs, J Geophys Res, 113(D9), D09202, doi:10.1029/2007JD009170.

Mishchenko, M., B. Cairns, J. Hansen, L. Travis, R. Burg, Y. Kaufman, J. Martins, et al., 2004: Monitoring of aerosol forcing of climate from space: analysis of measurement requirements. *J. Quant. Spect. & Rad. Trans.*, **88**(1-3), 149–161, doi:10.1016/j.jqsrt.2004.03.030.

Remer, L.A., R.G. Kleidman, R.C. Levy, Y.J. Kaufman, D. Tanre, S. Mattoo, J.V. Martins, et al., 2008: Global aerosol climatology from the MODIS satellite sensors. *J. Geophys. Res.*, **113**(D14), D14S07. doi:10.1029/2007JD009661.

Remer, L., Y. Kaufman, D. Tanre, S. Mattoo, D. Chu, J. Martins, R. Li, et al., 2005: The MODIS aerosol algorithm, products, and validation. *J. Atmos. Sci.*, **62**(4), 947–973.

Solomon, S., D. Qin, M. Manning, M. Marquis, K. Averyt, M. M. B. Tignor, H. L. Miller Jr., and Z. Chen, 2007: Climate Change 2007: The Physical Sciences Basis. Cambridge University Press, 996 pp.

Tanre, D., M. Herman, and Y. Kaufman, 1996: Information on aerosol size distribution contained in solar reflected spectral radiances. *J. Geophys. Res.*, **101**(D14), 19043–19060.

Tanre, D., Y. Kaufman, M. Herman, and S. Mattoo, 1997: Remote sensing of aerosol properties over oceans using the MODIS/EOS spectral radiances. *J. Geophys. Res.*, **102**(D14), 16971–16988.

Weatherhead, E. C., G.C. Reinsel, G.C., Tiao, X.L. Meng, X. L., D. Choi, W.K. Cheang, T. Keller, J. DeLuisi, D.J. Wuebbles, and J.B. Kerr, 1998: Factors affecting the detection of trends: Statistical considerations and applications to environmental data, Journal of Geophysical Research: Atmospheres (1984–2012), 103(D14), 17149–17161.

Winker, D. M., Pelon, J., Coakley, J. A. J., Ackerman, S. A., Charlson, R. J., Colarco, P. R., Flamant, P., Fu, Q., Hoff, R. M., Kittaka, C., Kubar, T. L., Le Treut, H., McCormick, M. P., Megie, G., Poole, L., Powell, K., Trepte, C., Vaughan, M. A. and Wielicki, B. A., 2010: The CALIPSO Mission: A Global 3D View of Aerosols and Clouds, *Bull. Am. Meteorol. Soc.*, 91(9), 1211–1229, doi:10.1175/2010BAMS3009.1.

Witte, J. C., A. R. Douglass, A. da Silva, O. Torres, R. Levy, and B. Duncan, 2011: NASA A-Train and Terra observations of the 2010 Russian wildfires, *Atmos. Chem. Phys.*, **11,** 9287-9301, doi:10.5194/acp-11-9287-2011.

Xiong, X., N. Che, and W.L. Barnes, 2006: Terra MODIS On-Orbit Spectral Characterization and Performance. *IEEE Transact. Geosci. Remt. Sens. 44*, 2198-2206.

Zhang, J., and J.S. Reid, 2006: MODIS aerosol product analysis for data assimilation: Assessment of over-ocean level 2 aerosol optical thickness retrievals. *J. Geophys. Res.*, **111**(D22), D22207. doi:10.1029/2005JD006898.

Zhang, J. and Reid, J. S., 2009: An analysis of clear sky and contextual biases using an operational over ocean MODIS aerosol product, Geophys Res Lett, 36(15), doi:10.1029/2009GL038723.

Zhang, J. and J.S. Reid, 2010. A decadal regional and global trend analysis of the aerosol optical depth using a data-assimilation grade over-water MODIS and Level 2 MISR aerosol products. *Atmos Chem Phys 10*, doi:10.5194/acp-10-1-2010.

Table 1. Summary of spatial sampling strategies illustrated in Figure 2 and summary of temporal averaging approaches.

Sample Name	Sample Width
Full Swath (FS)	~2300 km
Mid-Width (MW)	~800 km
Narrow (4 variants: N1, N2, N3, N4)	~380 km
Curtain (4 variants: C1, C2, C3, C4)	~10 km (width of MODIS pixel)

Averaging Strategy	Procedure
Sample-then-Average	Per orbit, sample the MODIS full swath at the indicated sub-swath Aggregate sub-sample to spatial grid Average aggregates to the desired time period (e.g., monthly, seasonal, annual)
Average-then-Mask	Per orbit, aggregate the MODIS full swath to spatial grid Average to the desired time period Use "sample-then-average" result for relevant sub-sample/temporal average to retain or exclude grid boxes visited in sub-sample

Figures

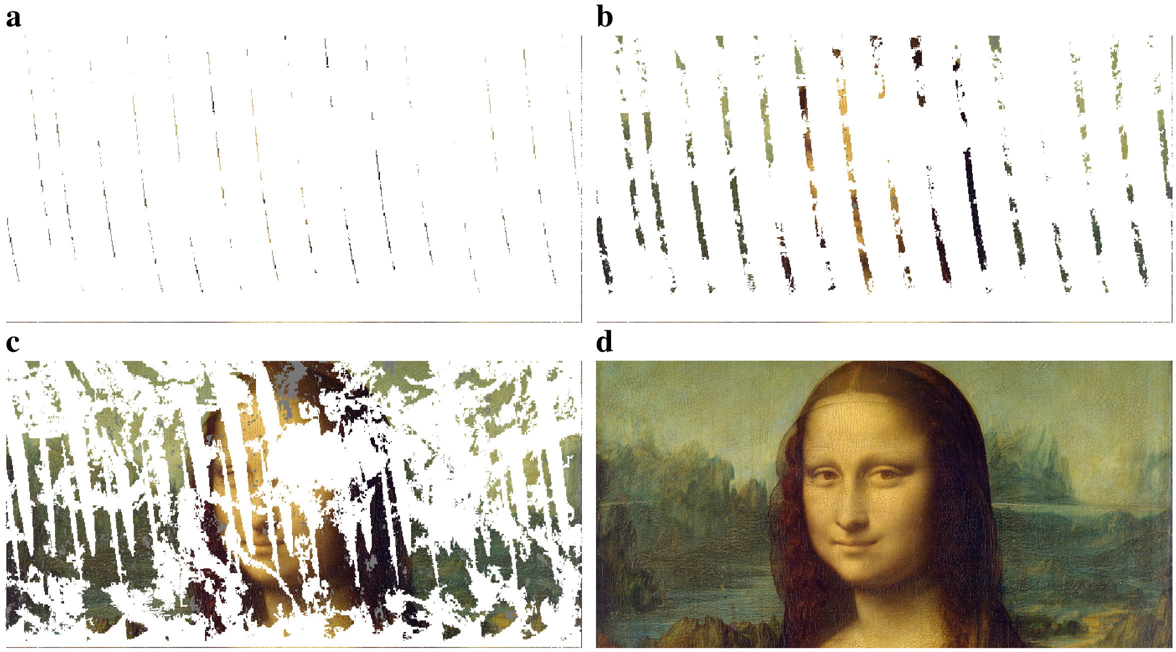

Figure 1. Conceptual illustration of the spatial sampling problem. Nature presents us with a “true” scene (d). The truth is sampled according to a “curtain” sampling (a), a “narrow” sampling (b), and the “full swath” sampling of the MODIS instrument on the Aqua spacecraft (c). For purposes of this illustration we are recovering only parts of the “true” image that had valid aerosol retrievals on June 5, 2010 from the MODIS over ocean and “dark target” land retrievals.

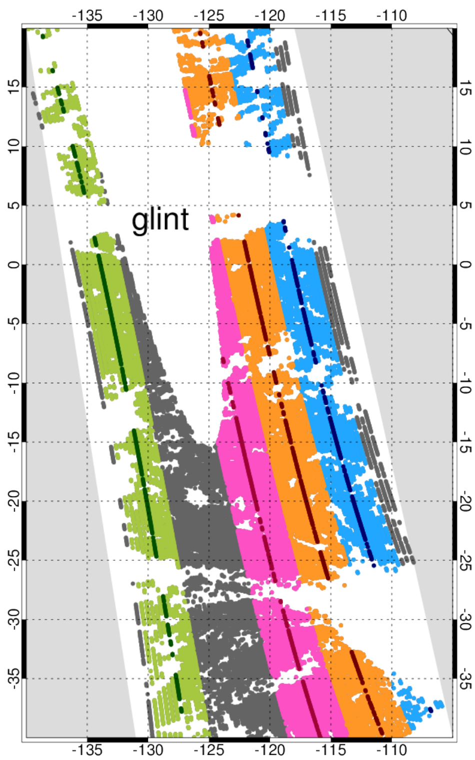

Figure 2. Example of spatial coverage of the MODIS Aqua instrument for an ocean region on June 5, 2010. The colored dots indicate the locations of the MODIS AOT retrievals, with the grey dots indicating the full MODIS swath (MO). Overlaid on the grey dots are different colors for our various sampling strategies (N1 = light blue, N2 = orange, N3 = magenta, N4 = light green, C1 = dark blue, C2 = dark red, C3 = deep purple, C4 = dark green, and MW = combined N1 and N2 swath). The light-grey shaded areas on the left and right side of the figure are outside the swath, while the central white region (labeled “glint”) is where no aerosol retrievals are made due to glint. Remaining patchy white areas are where aerosol retrievals were not made due to clouds.

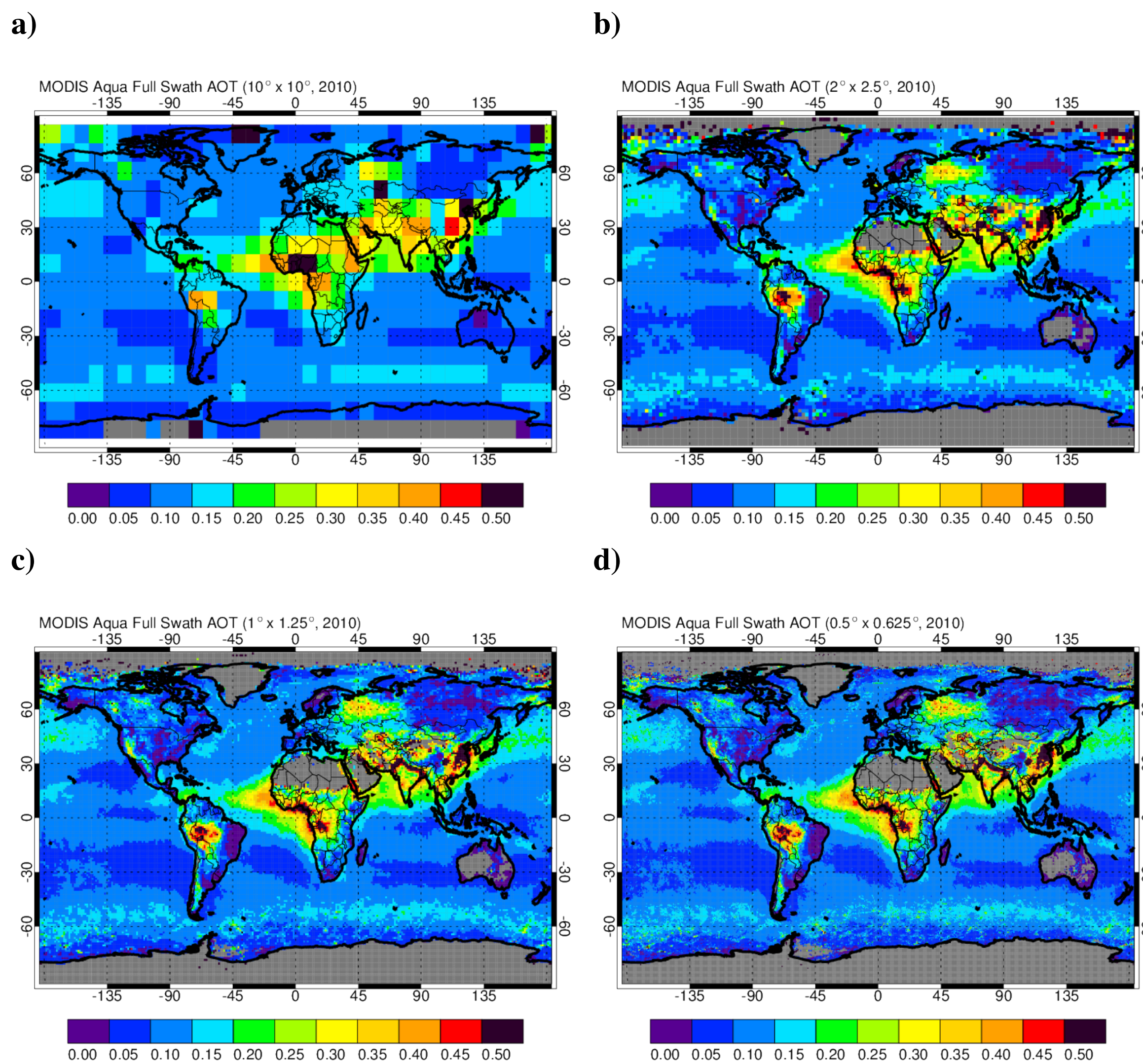

Figure 3. Full swath year 2010 annual mean AOT using the sampling and aggregation strategy in Equations 1 and 2 for each of our four aggregation resolutions: (a) 10° x 10°, (b) 2° x 2.5°, (c) 1° x 1.25°, and (d) 0.5° x 0.625°. The grey shading indicates locations where no MODIS AOT retrievals were made during the year.

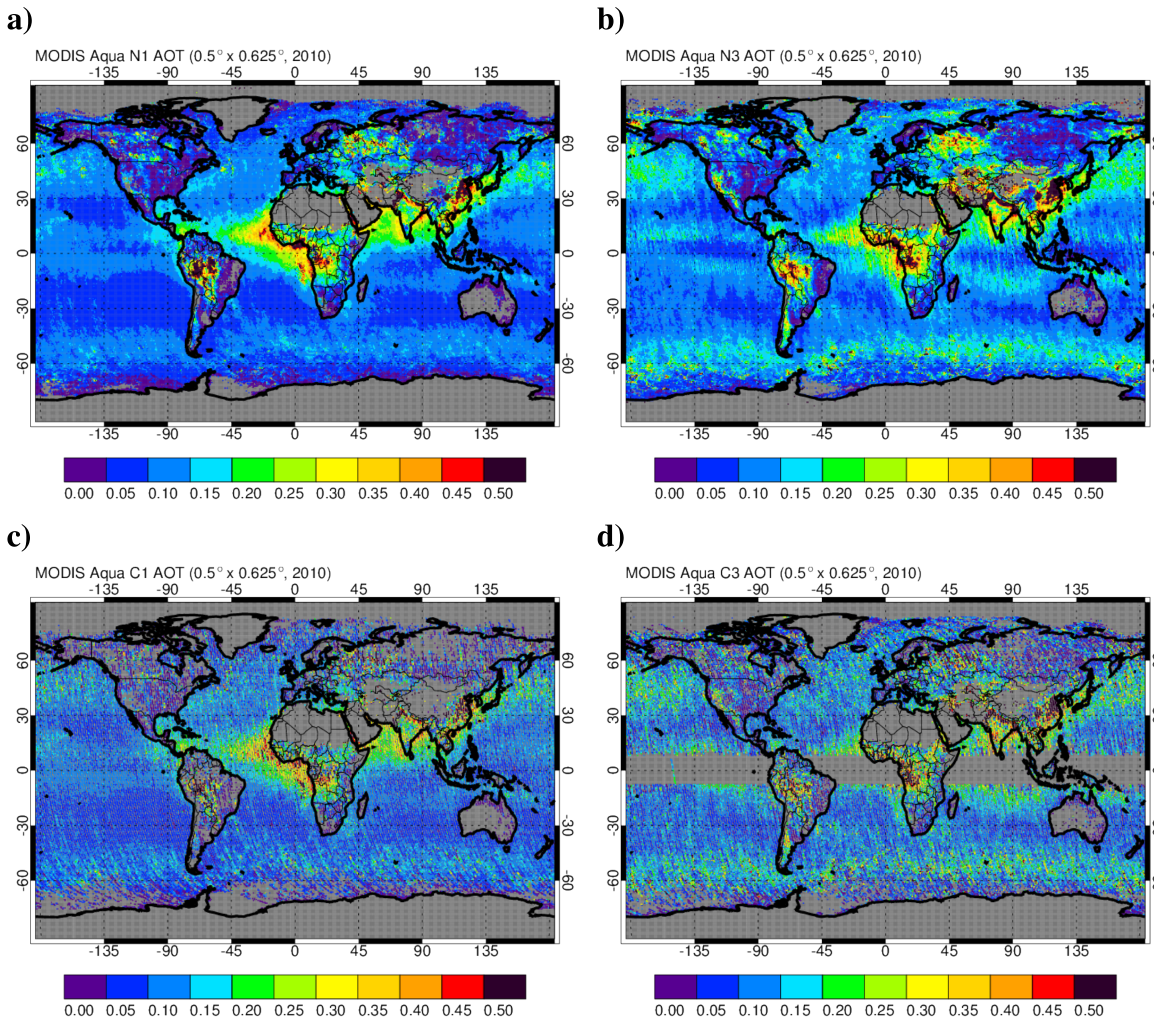

Figure 4. As in Figure 3, but at 0.5° x 0.625° resolution and for four of our sub-sampling strategies: (a) N1, (b) N3, (c) C1, and (d) C3.

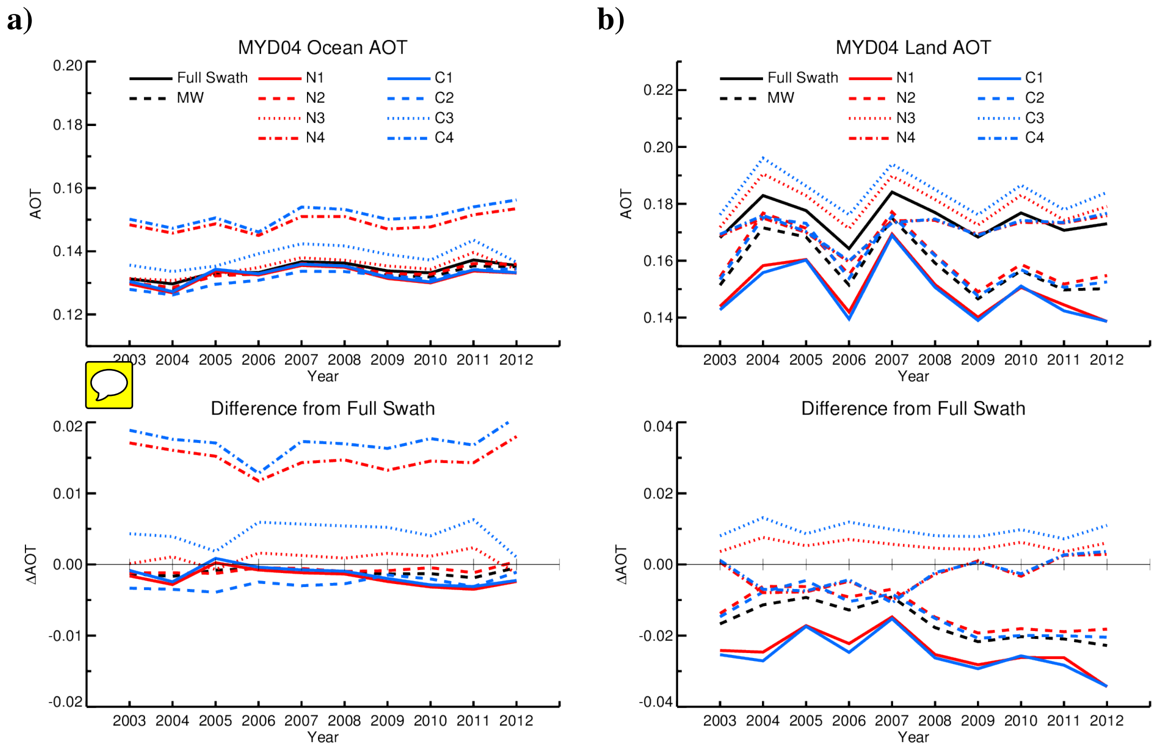

Figure 5. Years 2003 – 2012 time series of the global, annual mean MODIS Aqua AOT over ocean (a) and land (b). The solid black line indicates the full swath AOT, and the different colors and line styles indicate our different sampling strategies. The bottom panel in each is the difference of the sub-sampled average from the full swath average.

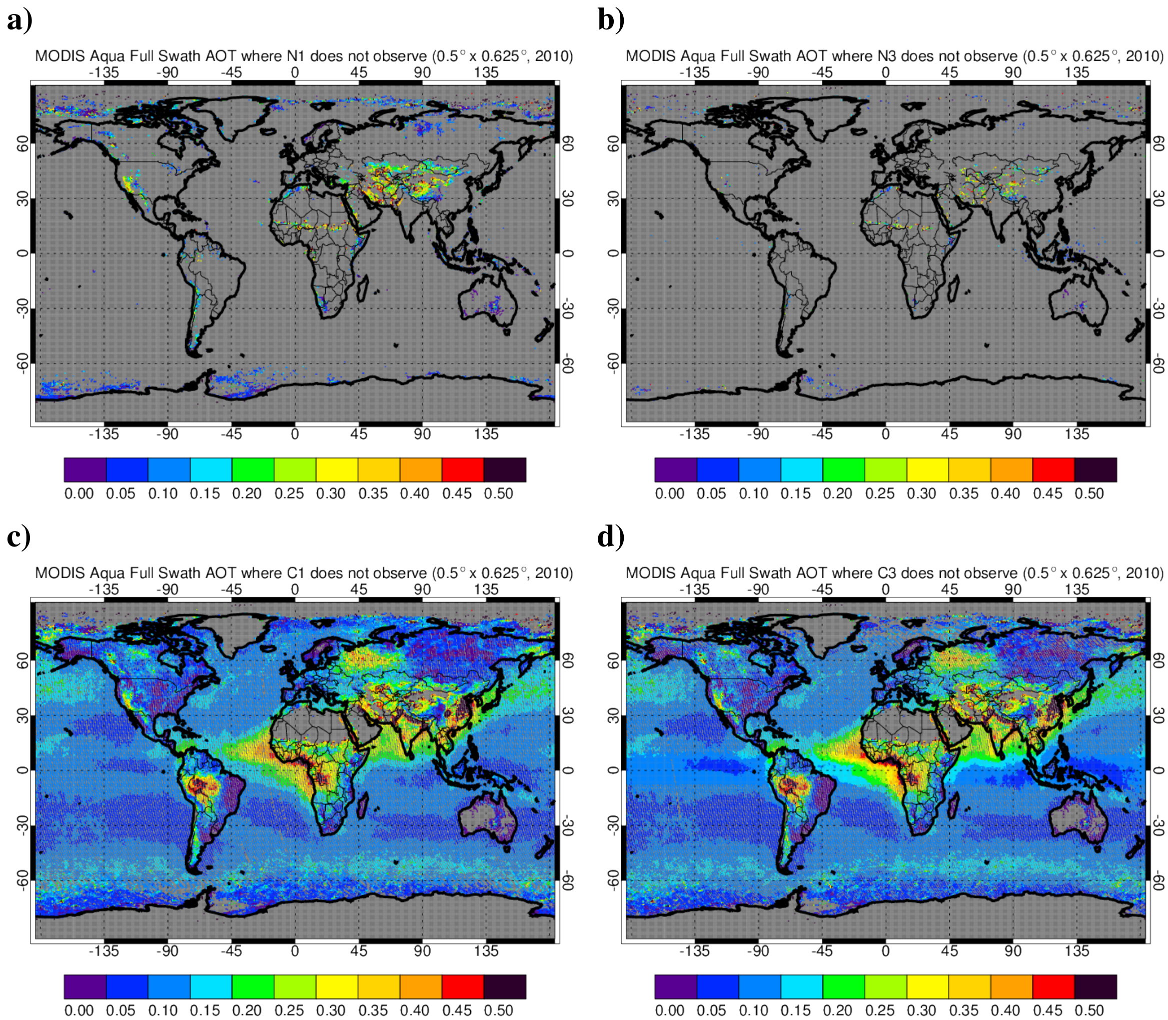

Figure 6. Full swath year 2010 annual mean AOT shown only at points never sampled by the indicated sub-sample swath: (a) N1, (b) N3, (c) C1, and (d) C3.

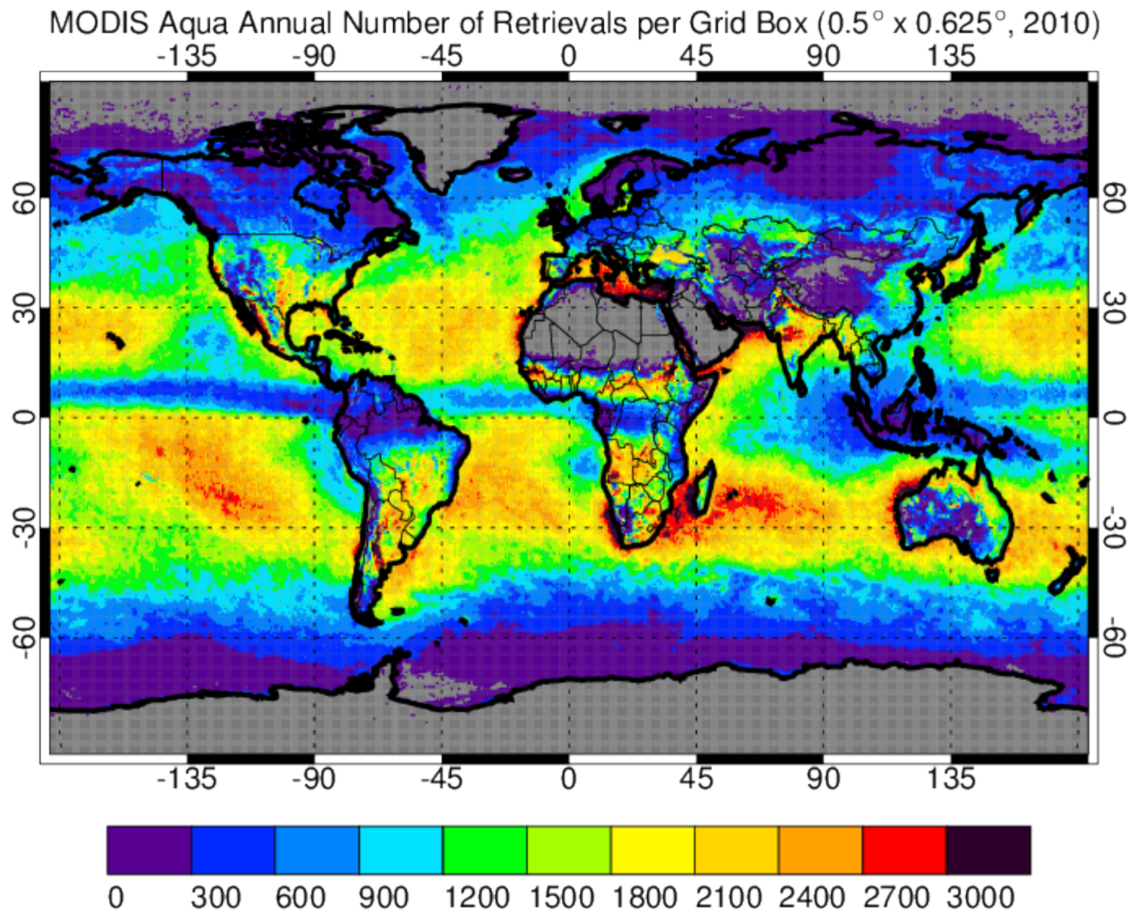

794 Figure 7. Number of MODIS Aqua AOT retrievals made per 0.5° x 0.625° grid box for

795 the entire year 2010 as used to compose the full swath annual mean shown in Figure 3d.

796

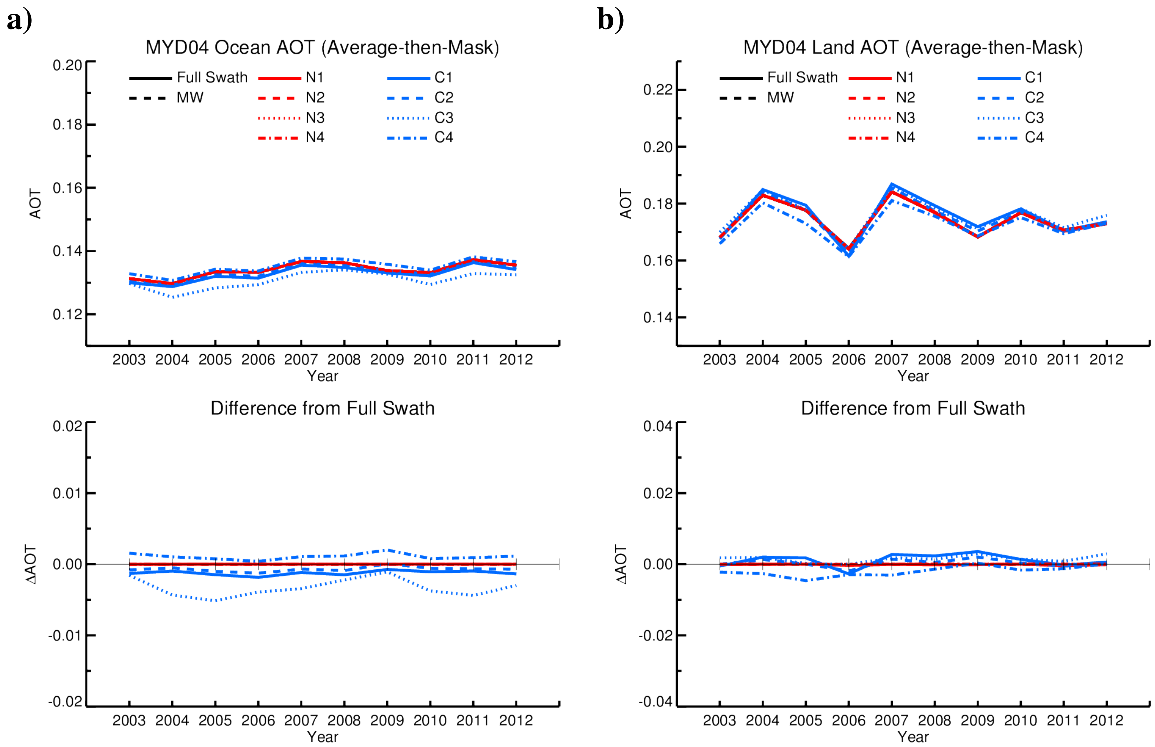

Figure 8. As in Figure 5, but now using the "average-then-mask" strategy to construct the annual means described in Section 3.2.

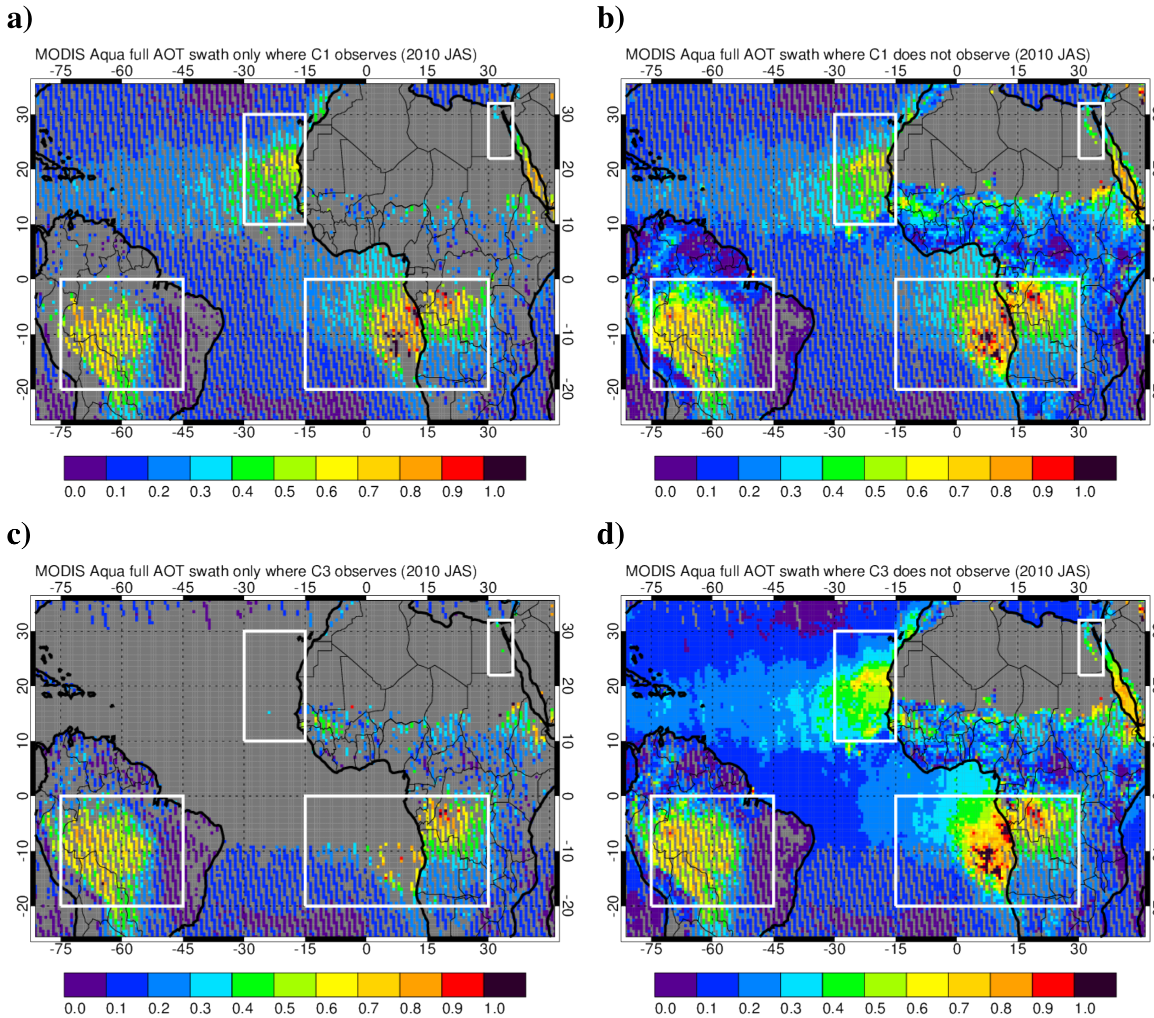

Figure 9. Full swath seasonal (July-August-September 2010) MODIS Aqua AOT over the tropical Atlantic Ocean. The full swath seasonal mean is masked to show only grid cells where the C1 and C3 sub-samples do (a, c) and do not (b, d) have a seasonal mean value. Figures 9a and 9c illustrate the “average-then-mask” seasonal mean AOT.

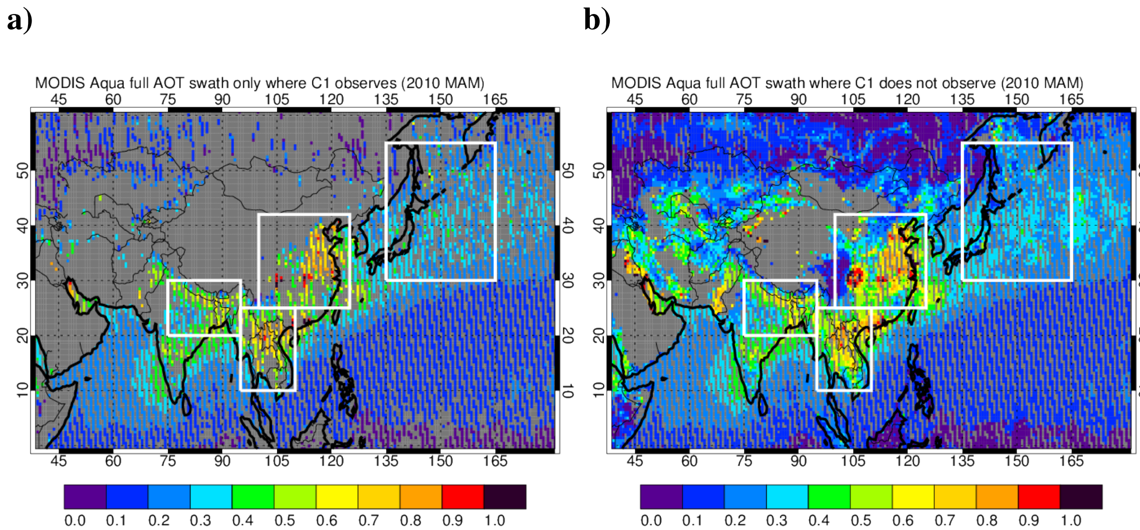

Figure 10. As in Figure 9, but for the C1 sub-sampling mask for March-April-May 2010 over Asia. The full swath seasonal mean AOT is shown both where the C1 sub-sample does (a) and does not (b) have a valid seasonal mean.

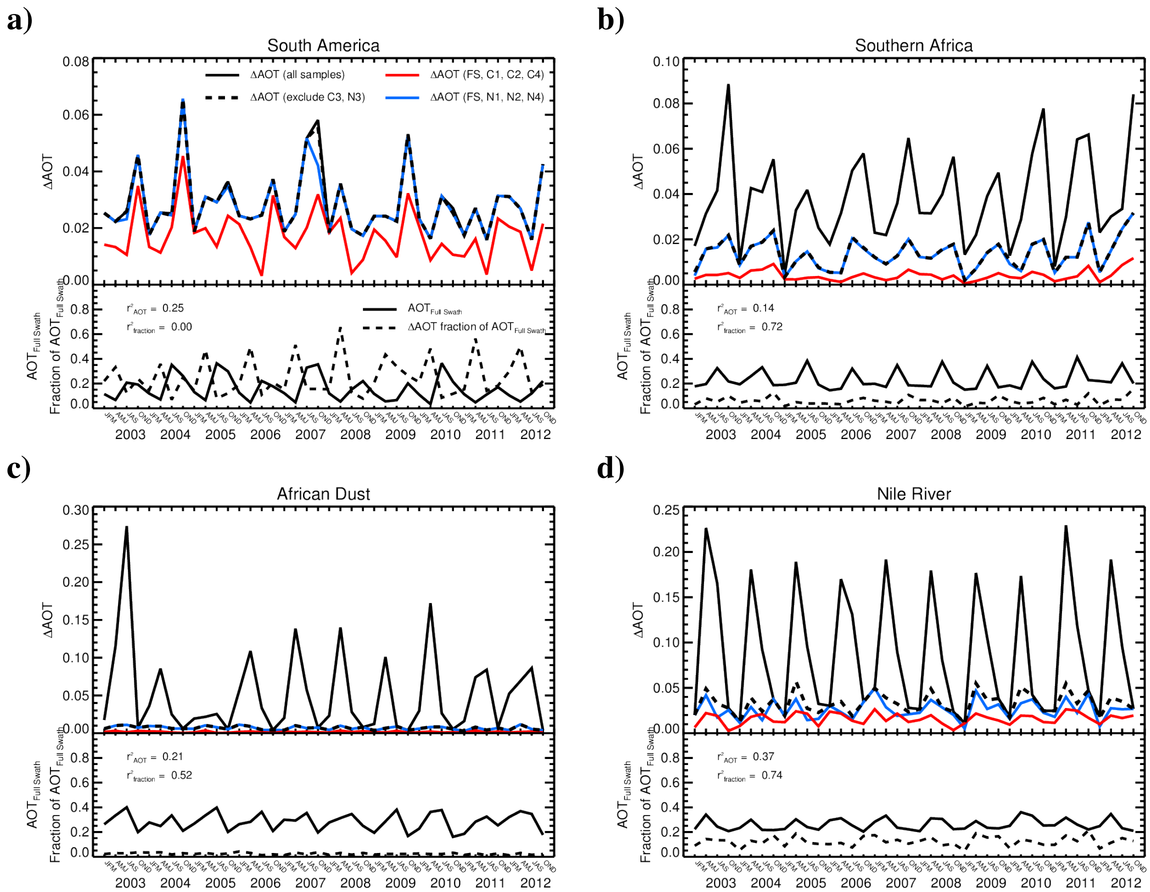

Figure 11. Seasonal-regional sampling artifact as ΔAOT between minimum and maximum AOT values for each sampling strategy (top, solid line) and for all but the C3 and N3 samples (top, dashed). For all, the "average-then-mask" sampling approach is used. The blue line is the ΔAOT computed using only the full swath, C1, C2, and C4 samplings. The red line is the ΔAOT using only the full swath, N1, N2, and N4 samplings. Also shown are the full swath mean AOT (bottom, solid line) and ΔAOT as a fraction of the full swath AOT (bottom, dashed). The r^2 correlation coefficient between the sampling artifact ΔAOT (in all cases, excluding C3 and N3) the full swath seasonal-regional mean AOT and the ΔAOT as a fraction of the full swath mean are also shown.

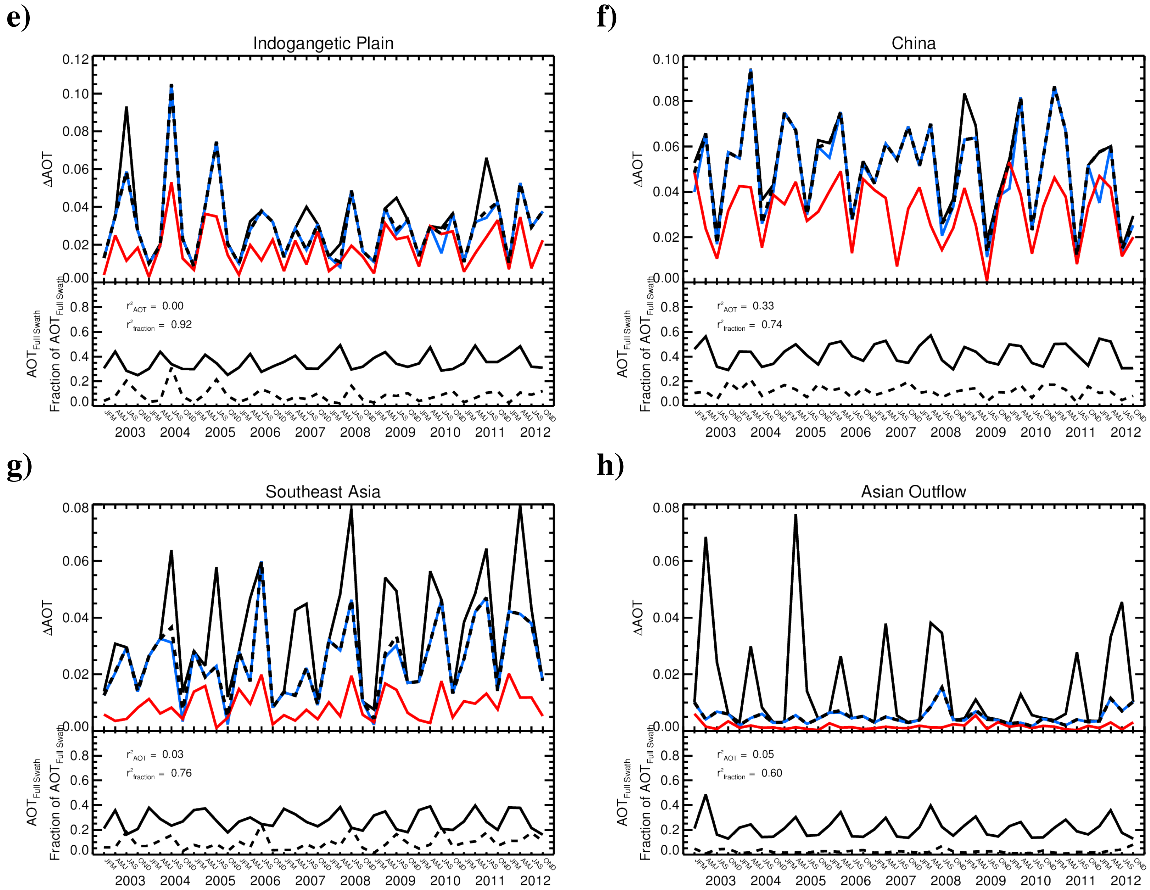

Figure 11 (continued).

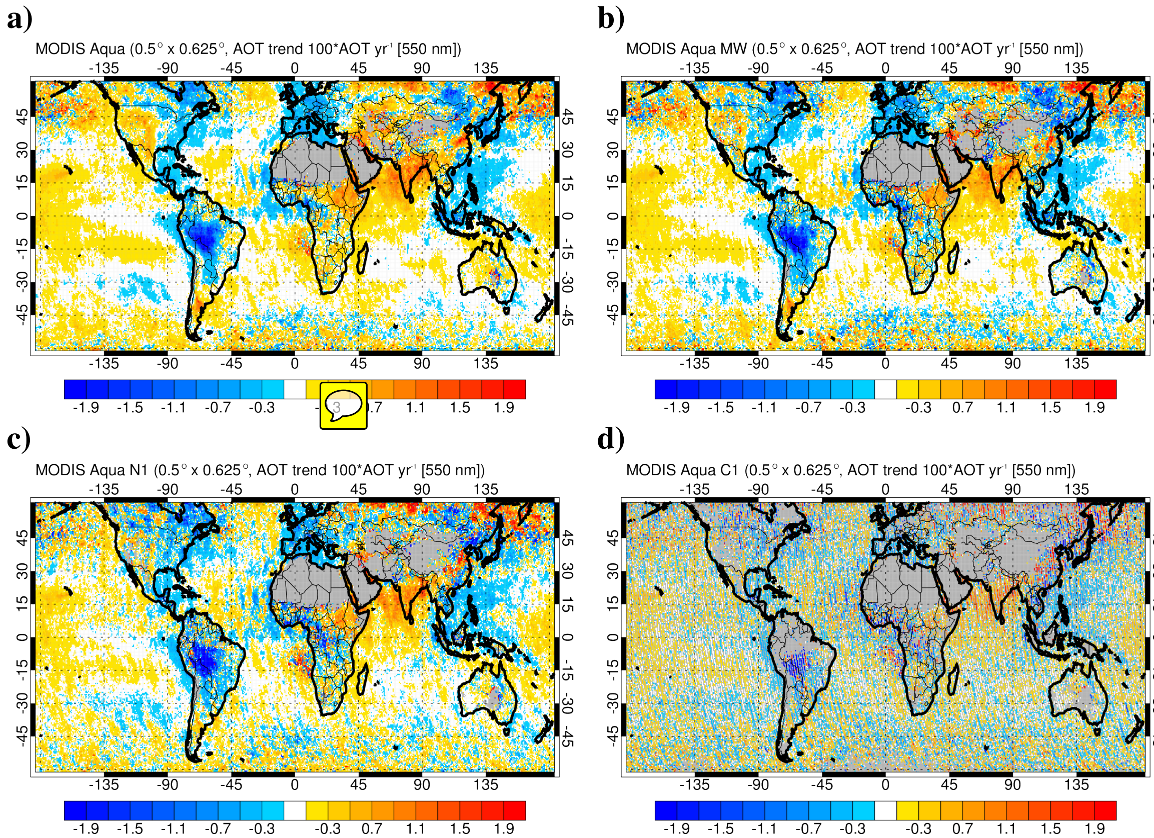

Figure 12. Trend for the ten-year (2003 – 2012) time series of MODIS Aqua AOT. We show the trend for the full swath (a), mid-width (b), N1 (c), and C1 (d) samplings. Grey areas are locations with either no valid retrievals or where the time series has fewer than 12 $month_n$ and $month_{n-1}$ pairs.

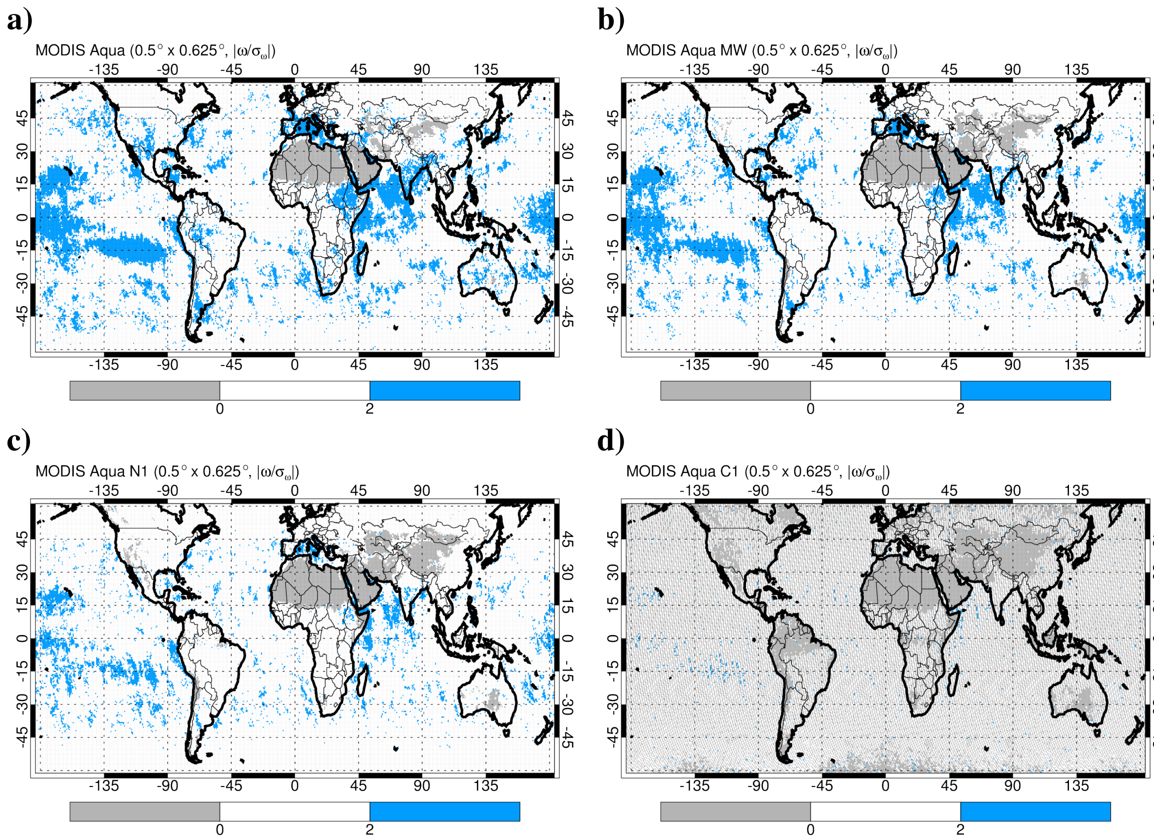

Figure 13. As in Figure 12, but showing the statistical significance for the trends shown in Figure 12. Regions colored blue (bottom plots) are showing statistically significant trends at the 95% confidence level.

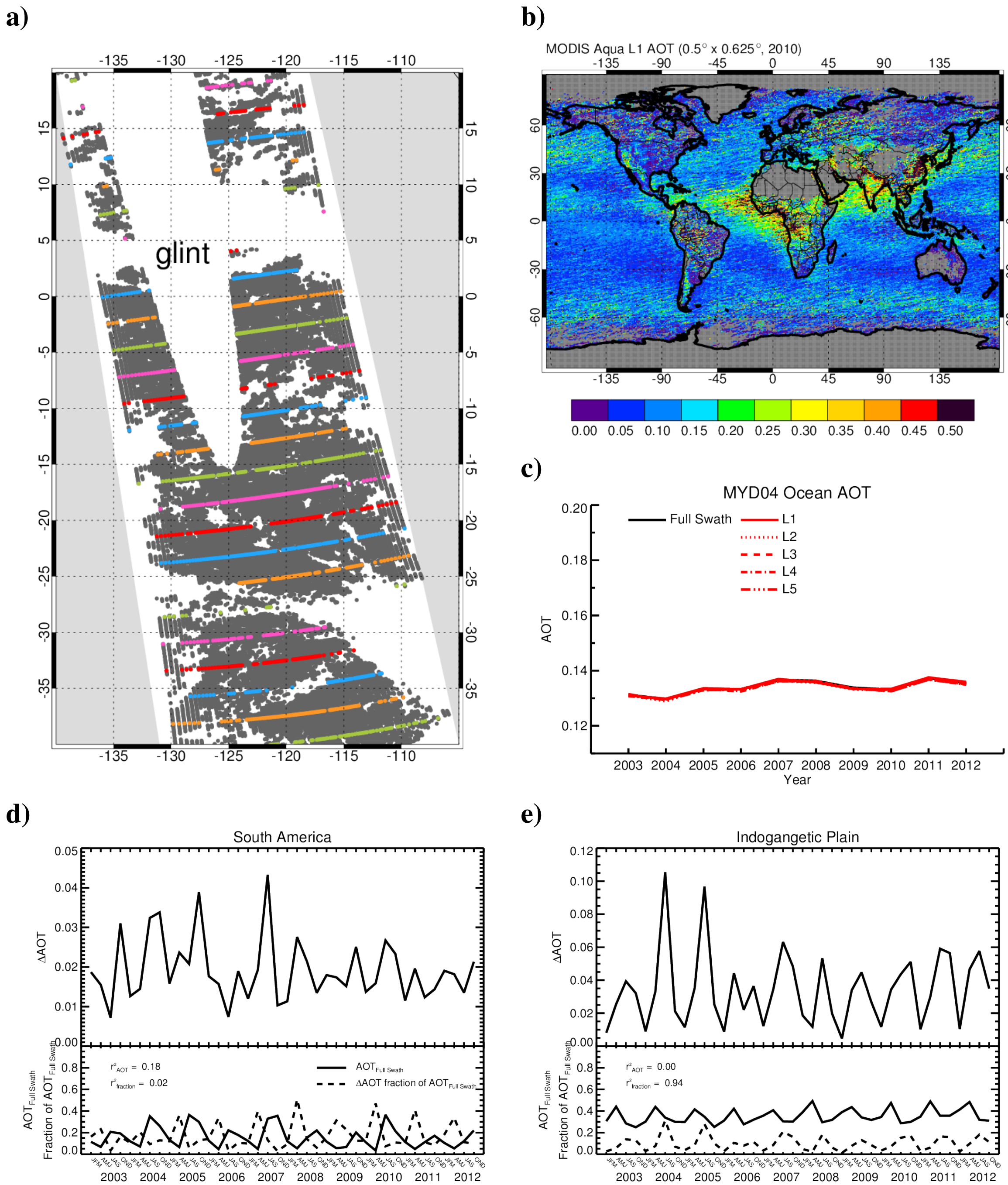

Figure 14. Examples from latitudinal (across-track) sampling exercise after Geogzhayev et al. (2013). (a) Sampling pattern for five latitudinal sampling strategies tried: L1 (blue), L2 (orange), L3 (green), L4 (magenta), and L5 (red) (compare with Figure 2). (b) Year 2010 annual mean AOT for L1 sampling (compare with Figure 3d). (c) Time series of global, annual mean AOT over ocean for full swath and all latitudinal samplings

(compare with Figure 5). The full swath annual mean AOT (black line) is obscured by the latitudinal sub-samples (red lines). Also shown are the ΔAOT sampling artifacts for two regions: South America (d) and the Indogangetic Plain (e) (compare with Figure 11).

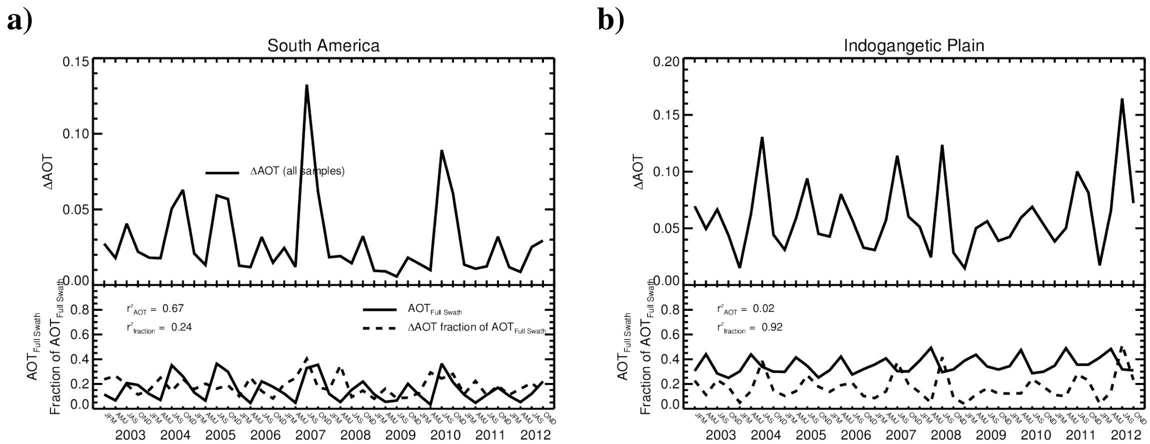

Figure 15. ΔAOT seasonal-regional sampling artifact for across-track latitudinal sampling using the “sample-then-average” approach for (a) South America and (b) Indogangetic Plain. Note the different y-axis scale from Figures 14d and 14e.

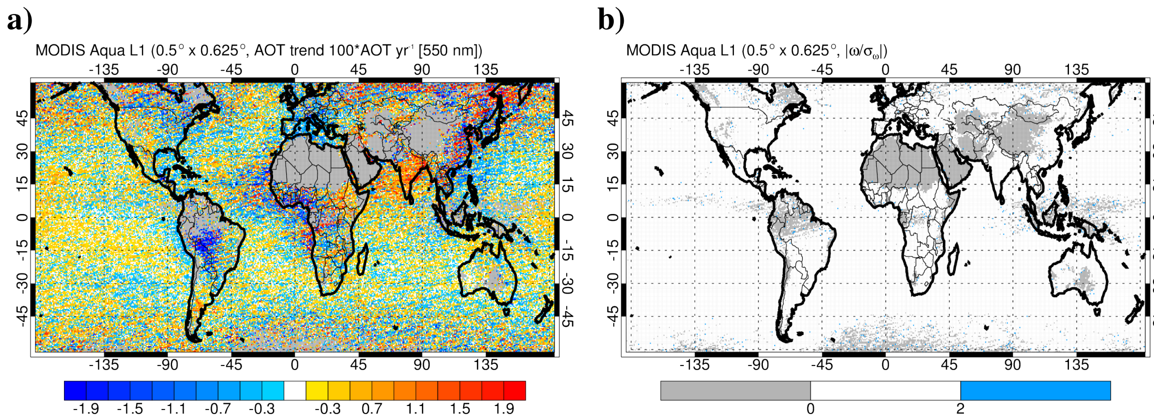

Figure 16. AOT trend (a) and statistical significance (b) for the L1 across-track sub-sample.

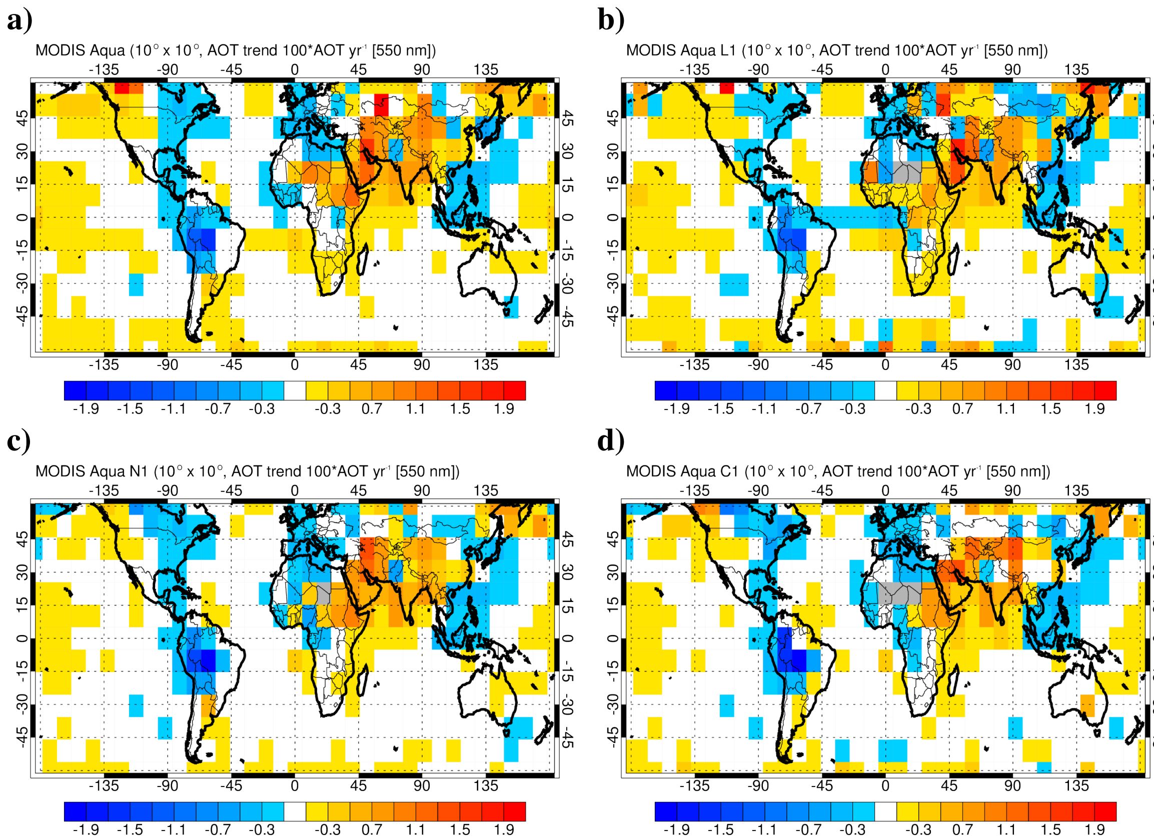

Figure 17. Aerosol trends for the full swath (a), L1 (b), N1 (c), and C1 (d) samplings at 10° x 10° aggregation resolution.

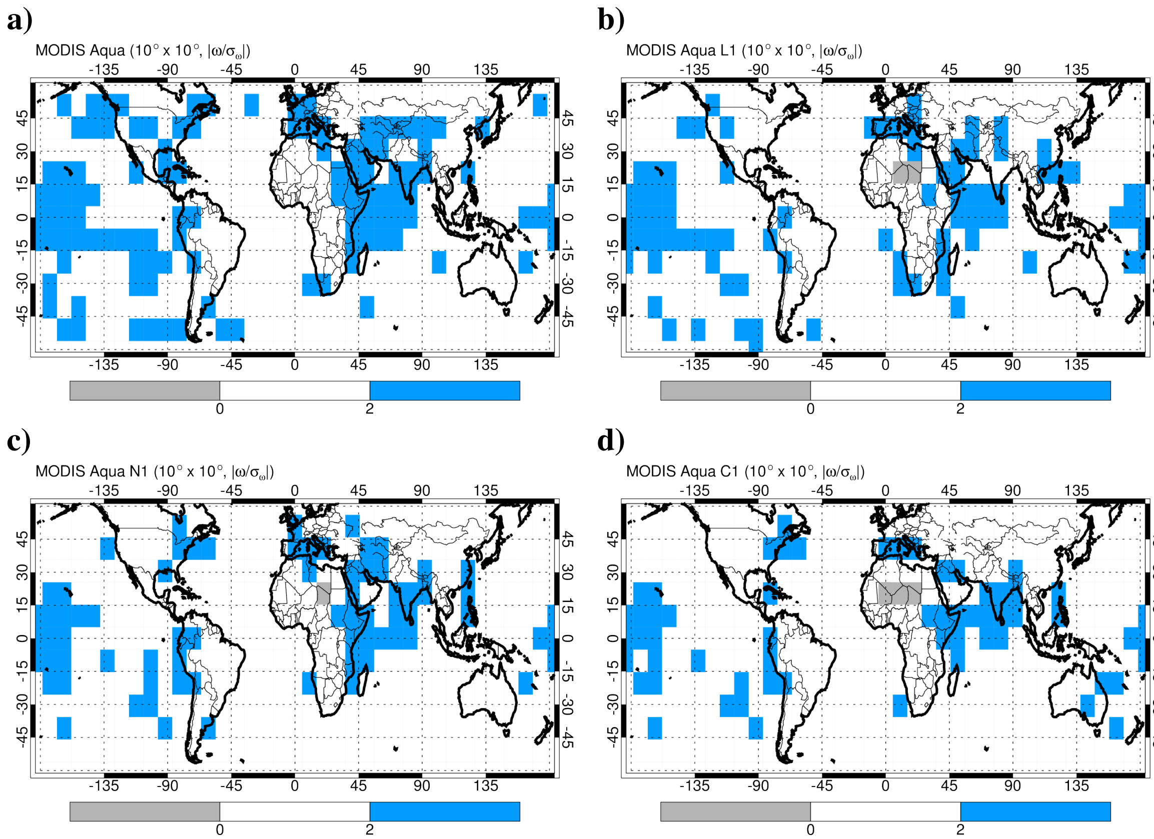

Figure 18. As in Figure 17, but for the 95% statistical significance interval.